CHALMERS

UNIVERSITY OF TECHNOLOGY

Torque Estimation Algorithms
for Stepper Motor

Master's Thesis in Electrical Engineering

JULIA JANSSON
CHARLOTTE RÅDAHL

Department of Electrical Engineering
CHALMERS UNIVERSITY OF TECHNOLOGY
Gothenburg, Sweden 2018

Torque Estimation Algorithms for Stepper Motor

Julia Jansson
Charlotte Rådahl

Department of Electrical Engineering
CHALMERS UNIVERSITY OF TECHNOLOGY
Gothenburg, Sweden

Torque Estimation Algorithms for Stepper Motor
JULIA JANSSON
CHARLOTTE RÅDAHL

Cover: Valve control system consisting of a butterfly valve, gearbox and 2-phase bipolar hybrid stepper motor.

Gothenburg, Sweden 2018

Torque Estimation Algorithms for Stepper Motor
JULIA JANSSON
CHARLOTTE RÅDAHL
Department of Electrical Engineering
Chalmers University of Technology

Abstract

Preventive health monitoring solutions of valve control systems for offshore applications are profitable due to possibility to plan maintenance work. Load torque is a good indicator of system health as it provides information to the user whether the controlling motor can generate enough torque to move the valve stem or if it is close to its limits. To do this it is desirable to avoid expensive and large torque sensors, opening up for the opportunity to investigate the possibility of estimating the torque on the load based on motor parameters. The motor under investigation is a 2-phase bipolar hybrid stepper motor with torque components from both the variable reluctance and the permanent magnet in the rotor. Measurements confirm neglecting the reluctance torque component to be acceptable, simplifying the derived motor torque expressions. Based on a Simulink model of the system developed from mathematical expressions regarding motor and load together with measured motor specific parameters, two motor torque estimation methods were developed and compared.

Simulations of the model were executed to estimate uncertainties in the load torque algorithm. The load torque estimate was in turn depending on motor torque algorithm simplifications in order to limit the number of sensors in a implementation while upholding a approved tolerable accuracy. An estimation of the load torque was presented based on the motor torque calculations derived from output power and the assumption of a constant speed. The error of this estimate during a worst case scenario is smaller than 13% having a total load torque above 2 Nm, a value continuing to decrease with an increased load torque. In an implementation of this algorithm, current sensors are the only necessary sensors while remaining parameters are extracted from the reference values. The current sensors are used in systems having a closed loop current control, making the suggested load torque estimation not requiring any added sensors in an implementation.

Acknowledgements

Contents

1

Introduction

1.1 Background

The stepper motor is a device generating a stepwise rotational motion, which has an advantage in applications where a precise position control is of importance [1]. A microcontroller determines the sequence to produce winding currents and consequently a magnetic field in different phases, creating a rotational movement of the motor shaft by defined steps [2]. A result of the microcontroller is the stepper motors ability to be well functioning as an open loop system. In a closed loop system the number of steps achieved by the motor could be counted and made sure to be exact, an option of accuracy however is not necessary in all applications [3].

Due to its capability of creating sequential steps, the stepper motor has found application in for example computerised numerical control machines (CNC) and disk drives [1, 4]. Another load controlled by a stepper motor could be a valve. In applications requiring a lightweight system the butterfly valve is of interest. The flow of fluids in a butterfly valve is regulated through a disk opening and closing through a quarter turn, with a rubber lining ensuring a minimisation of leakages. Every opening and closing will tear the valve and as the number of openings and closings depends on the application the valve lifetime is difficult to estimate. One option to determine the mechanical health of the valve is to measure the torque required to alter the position of the valve. A system with a preventive health monitoring method could prevent failures and limit subsequent material and economical damage. Furthermore, a product informing the user when reparation is required give rise to a new business model. The supplier can sell the product as a subscription instead of an one time cost, opening an opportunity to secure the relationship between the supplier and buyer by signing more extensive contracts. In addition, unnecessary substitution of valves can be prevented due to the increased knowledge of each products individual lifetime. Replacements could be planned and performed at a time most suitable for the company, an interesting solution concerning industries directed towards offshore applications such as oil rigs and ships due to the limited maintenance availability.

The torque produced by the motor to close and open the valve can be measured using a torque sensor. However, adding parts to the system also increase the number of damageable components. Together with increased cost and space it is therefore important to limit the number of system components. To minimise these factors, the torque could instead be estimated from the stepper motor. This is a favourable method as it would utilise the existing hardware and the estimator could

be implemented in the controller program, compared to the bulky torque sensor.

1.2 Aim

In this master's thesis a Simulink model of a specific stepper motor and load system is developed with motor parameters extracted through measurements. Based on the model at least two algorithms estimating the load torque without using torque sensors will be constructed. An evaluation of the load torque estimation will be performed, with respective algorithms compared to each other to establish the most suitable choice for the given valve control system.

1.3 Limitations

The design of the stepper motor, its controller and the valve will not be altered or optimised with respect to the scope of this thesis. Neither will considerations regarding different materials going through the valve be taken into account, and thereby their effects on the system behaviour. This due to that all system components are not, in the beginning of the project, decided by the company.

The system will be modulated to consider a specific stepper motor. However, by changing the motor specific parameters the model can be applied to other stepper motors.

The remote diagnosis application of the system where the load torque estimation algorithms are developed in an embedded application, will not be designed in this thesis. The conclusions will be based on results provided by a simulation environment and verification in a real system will not be performed.

2
Valve Control System

This master's thesis regard a valve control system consisting of a butterfly valve controlled by a stepper motor. A schematic of the valve control system is shown in Figure 2.1. The figure shows a power supply that feed a DC voltage to a drive circuit regulated by a control circuit. Depending on the controller signals the windings of the 2-phase stepper motor are energised in a specific order. The energised phases A ($A+$, $A-$) and B ($B+$, $B-$) are seen in Figure 2.1 as a link between the drive circuit and the 2-phase stepper motor. The current in the windings generate a magnetic field which produce a torque that rotates the rotor. Through the gearbox the mechanical torque is transformed to a preferred rotational force. This up scaled force is used to open or close the valve and in turn control the flow. In the following sections the components of the valve control system are described more in detail.
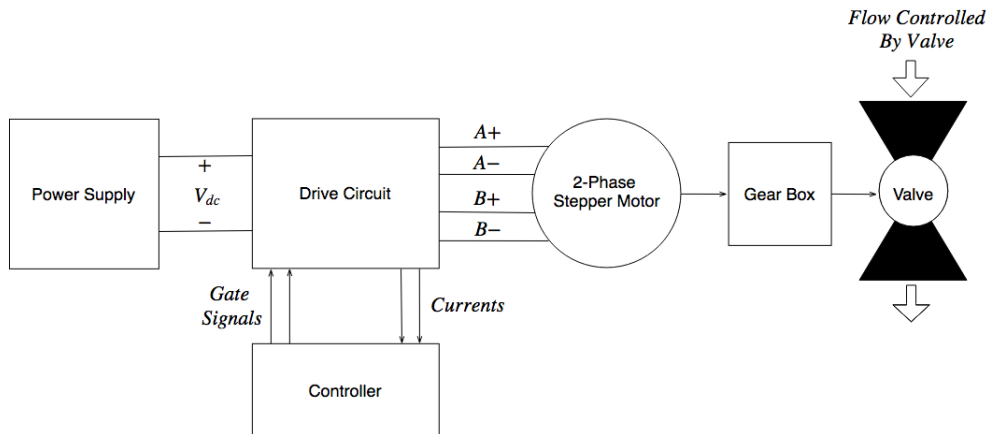
Figure 2.1: System components together with significant signals and their direction.

2.1   The Stepper Motor

The stepper motor is defined as a polyphase synchronous motor with both stator and rotor having teeth consisting of a magnetic permeable material, making the stepper motor salient as the source of flux depend on the rotor angular position [3, 5]. Shown in Figure 2.2 is the construction of the rotor, where the teeth, motor shaft and the polarities are defined. With an advantage of low cost and high reliability the stepper motor is additionally well functioning in open loop systems [2, 5]. As

the name implies the stepper motor generates a stepwise rotational movement of the motor shaft. The motor drive is regulated by a controller designed to transmit logic signals to create the most suitable stepwise rotation for the given application [6].
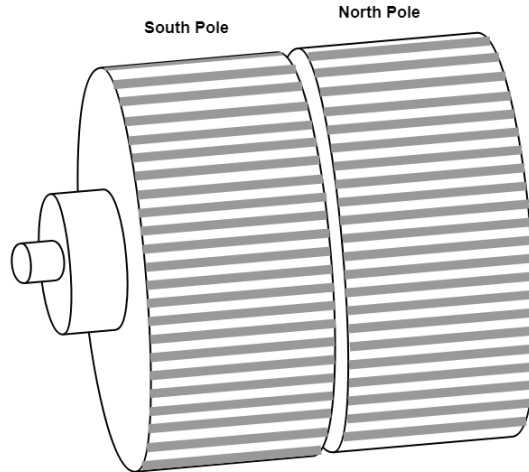
Figure 2.2: Construction of the hybrid stepper motor rotor. The opposite polarity of the permanent magnet rotor can be noted as well as the rotor shaft and the grey rotor teeth.

The variable reluctance, permanent magnet and a mixture of the two, called hybrid, are the three most common types of stepper motors. A hybrid stepper motor practice both the source of flux principle from the variable reluctance motor together with the principle of the permanent magnet. Applying the principle from the permanent magnet, the flux components considers both the stator and the permanent magnets in the rotor [2]. With a current through the stator windings the stator teeth are polarised. As a result of their polarisation and the permanent magnets in the rotor, a field between the windings and rotor teeth occur moving the rotor. Consequently the torque depend on the field strength resulting from the flux components, and the angle between the fluxes [2]. Observed in Figure 2.3 is the distribution of the rotor teeth of a hybrid stepper motor. Energising phase B so that B+ becomes a north pole, and B- a south pole, will attract the rotor teeth and lock the position shown in Figure 2.3. Based on that position, energising phase A so that A+ has a north polarity and A- becomes a south pole will create a counterclockwise rotational force, aligning the closest south tooth with the positive A-phase and the closest north tooth with the negative A-phase.

A variable reluctance motor instead use the principle of reluctance to generate torque. Ohm's law for magnetic circuits is expressed as

$$mmf = \Psi\Re, \tag{2.1}$$

and describes the relation between the magnetic field force mmf, the magnetic flux Ψ and reluctance $\Re$ [2]. Reluctance is a magnetic property equivalent to resistance in electrical circuits, i.e. the magnetic flux will flow through the path with least magnetic reluctance [7]. The working principle of the contribution from the reluctance motor can be described by neglecting the magnetic poles in Figure 2.3, i.e.
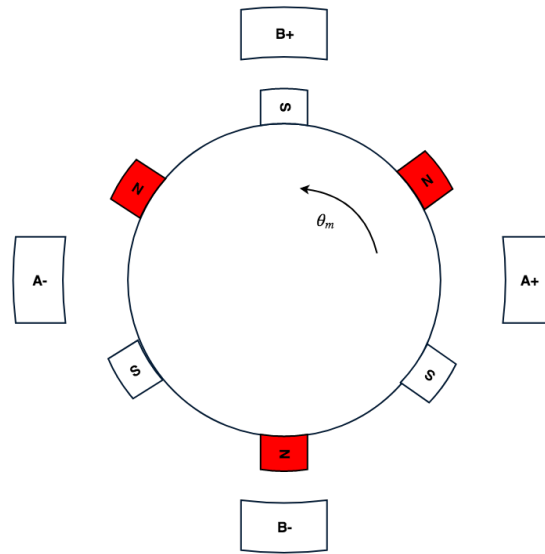
Figure 2.3: Phase distribution of the rotor of a hybrid stepper motor. The figure shows the rotor edge coinside with the shaft.

assuming the rotor not to be magnetised. The rotor is constructed of a permeable material, therefor if phase B is energised, the rotor would be locked to the position shown in the figure as the position provides the smallest air gap between the stator and rotor teeth, resulting in a lower reluctance compared to the reluctance in a larger air gap [2, 8]. If instead a current is applied to phase A the rotor would turn either clockwise or counterclockwise in order to align the rotor teeth with phase A. However, with the simple motor structure provided by Figure 2.3 the rotational direction can not be determined since the distance between the closest rotor teeth and the A phase is equal.

A hybrid stepper motor use both the characteristic of the permanent magnet motor together with the variable reluctance stepper motor. It therefor use the aspiration from the permanent magnet rotor teeth to attract or repel the excited windings as well as creating a rotation in order to minimise the air gap between stator and rotor, and thus obtain minimum reluctance [9, 10]. For applications requiring high motion resolution a small step angle of the rotor is desired, as it denotes the smallest individual rotational movement. Concerning systems employing larger angular steps the variance reluctance stepper motor is profitable and for applications requiring smaller steps the hybrid stepper motor is advantageous [3].

The corresponding static torque curve to Figure 2.3, used to describe the behaviour of the stepper motor, is shown in Figure 2.4, where the individual static torque of each phase is illustrated together with the sum of the phase torque components. The curve is obtained by altering the rotor position with mechanical angle θ_m and measure the torque generated by each phase at the given angle [10]. Both current direction and timing in the winding determine the performance of the stepper motor and the total system, making the maximum torque limited with less winding current [2]. Respective phase torque components shown in the figure are

described as

$$\tau_A = \tau_{kA}cos(\theta_m) = kI_Acos(N_1\theta_m),$$
$$\tau_B = -\tau_{kB}sin(\theta_m) = -kI_Bsin(N_1\theta_m),$$
(2.2)

where $I_A = I_B = $ constant, k a scaling factor, θ_m is the mechanical rotor position at $0°$ in Figure 2.4, and N_1 is a constant depending on the motor design. For the example in Figure 2.4 N_1 is 3, for one mechanical turn the rotor position will be repeated three times. Each torque component contributes to the total torque as

$$\tau_{tot} = \tau_A + \tau_B.$$
(2.3)

Assuming a full alignment of phase B at $0°$ and consequently a $90°$ misalignment of phase A in the same position, phase B and A are positioned in equilibrium at $0°$ respectively $30°$ as shown in Figure 2.4. Equilibrium defines the position where the rotor and stator teeth are aligned [2], i.e. when the energised winding is aligned with the opposite polarity of the rotor as shown in Figure 2.3. At angle θ_k the highest torque component τ_k is generated. The component τ_k, also known as the motor pull out torque, is dependent on the motor speed [10]. Using a τ_k-speed curve the relation between maximum torque compared to the applied load torque at a given speed is expressed. Additionally presented in a τ_k-speed curve are the motor resonance and instability problems occurring at specific velocities [2]. Consequently, using a τ_k-speed curve additional motor behaviour and dependencies can be observed.
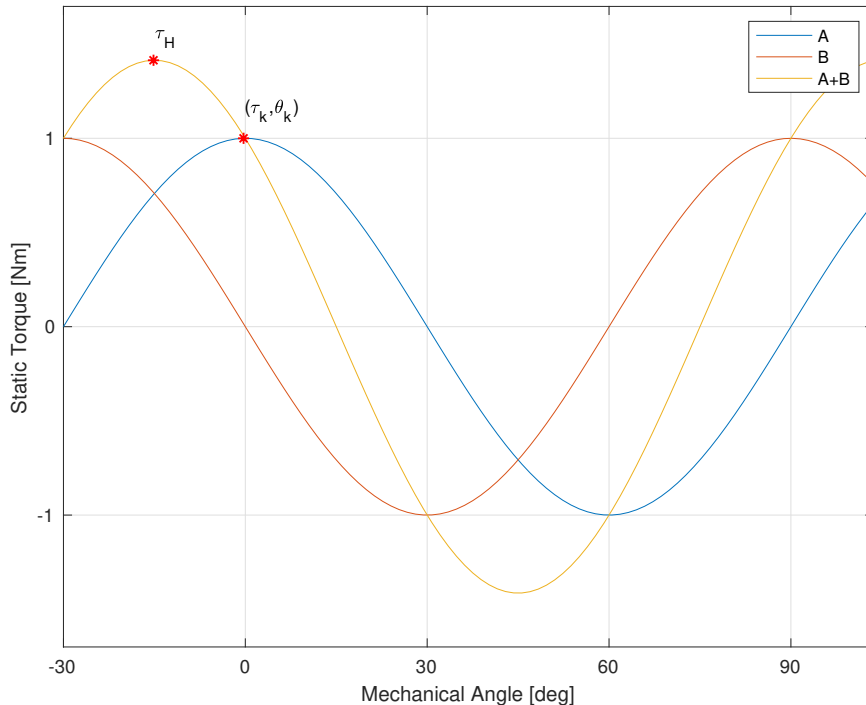
Figure 2.4: Static torque curve of 2-phase motor.

As torque is a result of the motor winding energisation the sequence and amplitude of the current fed to the windings are essential. The easiest stepping sequence

is single stepping where the rotor move in a number of distinct position during one electrical period [2]. The static torque curves shown in Figure 2.4 describe the torque components of the motor structure provided in Figure 2.3, whereas the position illustrated in Figure 2.3 refers to the static torque curves at 0 mechanical degrees. In that position winding B is fed a positive current, indicating phase B+ having a north polarity. At position 30°, a positive current is instead fed to winding A, moving the rotor another step counterclockwise. The two remaining movements of the electrical turn are performed by in turn energising winding B with a negative current, followed by an applied negative current in winding A at 60° respectively 90°. The described sequence is denoted as $B+, A+, B-, A-$ [10]. For every stepwise rotation of the rotor, the teeth will oscillate around the new position before settling. These oscillations can be viewed as a damped oscillating system and every new step will result in the same damped oscillations [10]. The step length is described by motor geometry according to

$$\text{step length} = \frac{360°}{N_r \cdot N_s}, \tag{2.4}$$

where N_r is the number of rotor teeth and N_s implies the number of phases in the stator [2]. The two states and six rotor teeth shown in Figure 2.3 result in a step length of 30°. Increasing the step resolution results in a smoother shaft rotation. After single stepping half stepping is the next level to an increased step resolution. Half stepping is introduced by repeating having one phase on and afterwards two phases on simultaneously [2].

To further increase step resolution the excitation mode microstepping is applied. As stepper motors with a high number of stator and rotor teeth are complicated to manufacture it is advantageous to divide the rotating steps into subsets. Such an action is achieved by applying winding currents unequal in amplitude while energising two phases simultaneously. This technique requires a closer surveillance as feedback to control varying motor parameters such as temperature [2]. With a position dependent current expressed as

$$\begin{aligned} I_A &= \hat{I}sin(\theta_e), \\ I_B &= \hat{I}cos(\theta_e), \end{aligned} \tag{2.5}$$

the current together with (2.3) is altered as

$$\tau_{tot} = kI_A sin(\theta_m) + kI_B cos(\theta_m) = k\hat{I}cos(\theta_m - \theta_e), \tag{2.6}$$

creating a motor torque dependent on both electrical position, θ_e, and mechanical rotor position, θ_m, resulting in an increased stepping resolution.

Adding a load torque result in an angular displacement of the equilibrium position and misalignment of the rotor and stator, a disadvantage associated with the stepper motor [2]. This step position error is inevitable, but by designing a steep curve around the step position the effects are decreased. Choosing a motor with higher τ_k than necessary is another option to increase the steepness of the curve, separating the actual curve from the sinusoidal approximation [2].

The holding torque τ_H is the maximum achievable torque produced by the motor before it starts an uncontrolled continuous rotation. This parameter is important as it provides an overall estimation of the system capability [2]. As shown in Figure 2.4 the total torque produced by the motor at a given rotor angle is a sum of the individual phase contributions. For a two phase motor τ_H is derived from τ_{kA} and τ_{kB} as [10]

$$\tau_H = \frac{1}{\sqrt{2}}\tau_{kA} + \frac{1}{\sqrt{2}}\tau_{kB} = \sqrt{2}\tau_k, \tag{2.7}$$

hence τ_k is defined as the effective value of τ_H.

2.1.1 Hybrid Stepper Motor

Since a variance reluctance stepper motor require at least three phases while the investigated valve control system is designed to use a two phase stepper motor, a hybrid stepper motor is consequently studied in this project [5]. The hybrid stepper has the combined ability of both permanent magnet and variable reluctance stepper motor. The stator is divided into poles, each with a surrounding coil [10]. As the rotor of the hybrid stepper is a cylindrical permanent magnet with opposite polarised edges it react to the produced magnetic field which results in a rotational movement. An overview of the rotor is shown in Figure 2.2, where the structure and polarisation distribution is defined. In order to provide a controllable stepwise rotation of the rotor, the rotor and stator poles are divided into small sections i.e. teeth, which are noticeable in Figure 2.2. Shown in the figure, the misalignment of the north and south rotor teeth is 90°.

A motor with four stages of phase excitation as shown in Figure 2.4 the relation of step length described in (2.4) is reduced to [3]

$$\text{step length} = \frac{90°}{N_r}, \tag{2.8}$$

an equation true for all 2-phase bipolar hybrid stepper motors. With $N_r = 50$, one mechanical turn of a 2-phase stepper motor is the result of 50 teeth alignment periods. With one teeth alignment period being equal to one electrical period $\theta_e = \frac{360°}{50} = 7.2°$ making one electrical period consisting of 4 steps making one step length 1.8°. The mechanical angle in relation to the electrical angle is thereby derived as $\theta_e = 50 \cdot \theta_m$, indicating that one mechanical turn is translated into 50 electrical periods. For a hybrid stepper motor the typical step length is 1.8° which provide a higher angular position resolution compared to a variable reluctance motor [3].

2.1.2 Electrical Model Of The Hybrid Stepper Motor

The electrical model of the hybrid stepper motor refer to the winding circuit illustrated in Figure 2.5. The figure shows a simplified schematic of a basic winding circuitry where the electric dynamics are mathematically described as

$$v_j = Ri_j + e_j, \tag{2.9}$$

with R being the winding resistance, v_j the applied phase voltage, i the system current and e_j the EMF for a specific phase j. The induced voltage depend on the flux linkage as

$$e_j = \frac{d\Psi_j}{dt}, \tag{2.10}$$

consisting of both the winding inductance voltage and the induced back-EMF, e_{b_j}, seen in Figure 2.5.
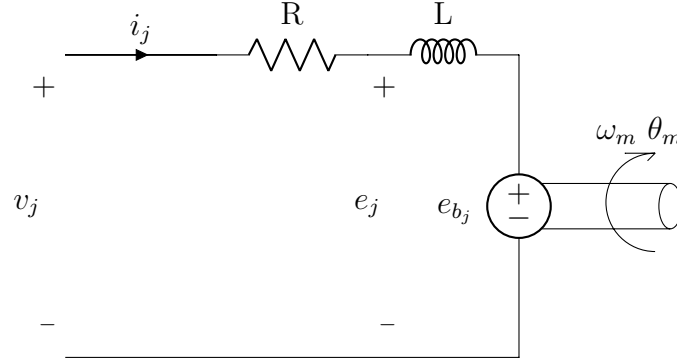
Figure 2.5: Circuitry of the stator windings, where resistance, inductance, EMF and back-EMF are present, in addition to the winding applied input voltage and the resulting winding current.

For a 2-phase stepper motor the total flux linkage in phase A and B are described as

$$
\begin{aligned}
\Psi_A &= L_A(\theta_e, i)i_A + \Psi_M cos(\theta_e), \\
\Psi_B &= L_B(\theta_e, i)i_B + \Psi_M sin(\theta_e)
\end{aligned} \tag{2.11}
$$

where L_A and L_B are the position and current dependent inductance in winding A respectively B. The currents i_A and i_B flows in respective phase while Ψ_M is the maximum flux linkage from the permanent magnet through the winding. The angle of the electrical period is denoted θ_e. By combining (2.10) and (2.11) the phase A electrical dynamics are defined as

$$
\begin{aligned}
v_A &= Ri_A + \frac{d\Psi_A}{dt} \\
&= Ri_A + \frac{d}{dt}\left(L_A(\theta_e, i)i_A + \Psi_M cos(\theta_e)\right) \\
&= Ri_A + L_A(\theta_e, i)\frac{di_A}{dt} + i_A\frac{dL_A(\theta_e, i)}{dt} + \frac{d}{dt}(\Psi_M cos(\theta_e)) \\
&= Ri_A + L_A(\theta_e, i)\frac{di_A}{dt} \\
&\quad + i_A\left(\frac{\partial L_A(\theta_e, i)}{\partial \theta_e}\frac{\partial \theta_e}{\partial t} + \frac{\partial L_A(\theta_e, i)}{\partial i}\frac{\partial i}{\partial t}\right) - \Psi_M\omega_e sin(\theta_e).
\end{aligned} \tag{2.12}
$$

The electrical dynamics for phase B is determined in the same manner and expressed as

$$
v_B = Ri_B + L_B(\theta_e, i)\frac{di_B}{dt} + i_B\left(\frac{\partial L_B(\theta_e, i)}{\partial \theta_e}\frac{\partial \theta_e}{\partial t} + \frac{\partial L_B(\theta_e, i)}{\partial i}\frac{\partial i}{\partial t}\right) + \Psi_M\omega_e cos(\theta_e). \tag{2.13}
$$

As a result of the permanent magnet in the hybrid stepper rotor there exists a magnetic force unaffected of the winding energisation called detent torque τ_d [11]. Shown in Figure 2.6, τ_d exists between the stator and rotor adjacent teeth where the latter attracts the former due to reluctance. With one electrical period being 7.2° of one mechanical period, as described in Section 2.1.1, together with a step length of 1.8°, there exist four steps within a period. One electrical period start with rotor and stator teeth being aligned as shown in Figure 2.6 and ends when the rotor teeth has moved four quarters.
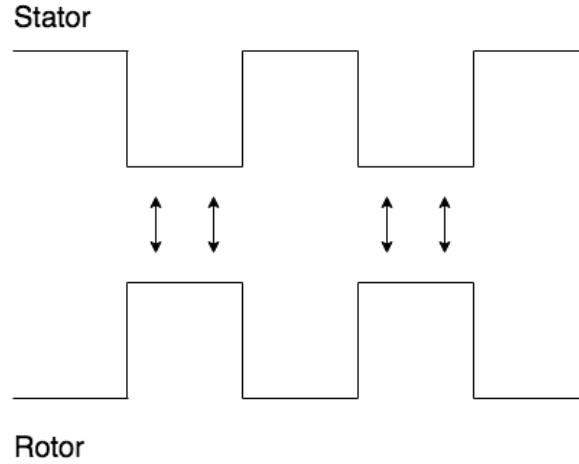
Figure 2.6: Full alignment of stator and rotor teeth.

One electrical turn will therefor result in four positions where the detent torque is maximal as shown in Figure 2.7. An assumption of a periodical detent torque is due to the expectation of the teeth being equally separated. The detent torque is defined as [12]

$$\tau_d(\theta_e) = A_d sin(4\theta_e), \tag{2.14}$$

with A_d being the amplitude of the position dependent detent torque.

2.1.3   Mechanical Model Of The Motor And Load

The mechanical model of a motor is derived from its mechanical dynamics. Concerning a hybrid stepper motor the mechanical dynamic structure is set as

$$\begin{aligned}
\frac{d\omega_m}{dt} &= \frac{1}{J}(\tau_e - \tau_d(\theta_m) - \tau_l), \\
\frac{d\theta_m}{dt} &= \omega_m,
\end{aligned} \tag{2.15}$$

with J being the motor inertia, τ_e, $\tau_d(\theta_m)$ and ω_m the electrical torque, detent torque depending on the mechanical rotor angle and the mechanical speed respectively [12]. A mathematical development of τ_e is provided in Chapter 3. Torque component τ_l is the load torque of the system, generated by the valve, the gear box and other mechanics in between [12].
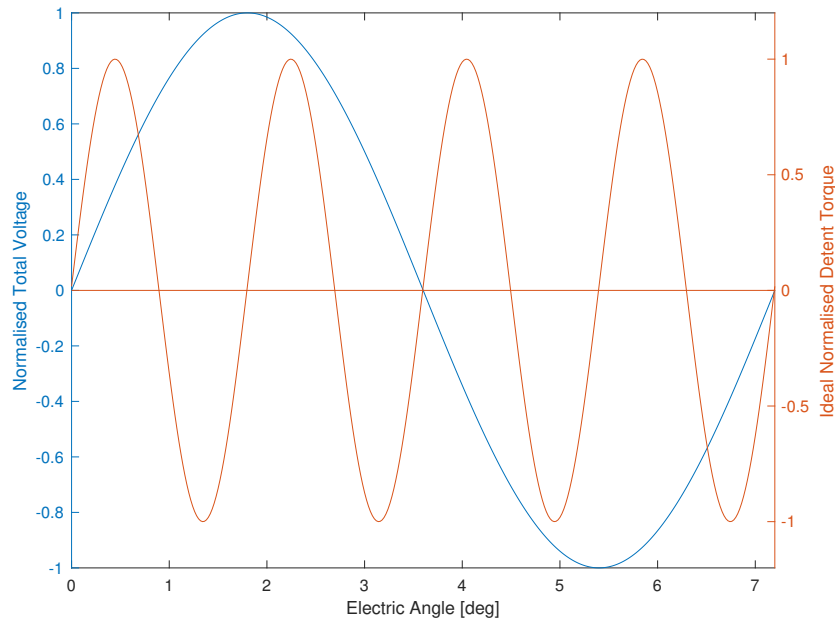
Figure 2.7: Wave form of the normalised detent torque and normalised total phase voltage over one electrical period.

2.2   Controller and Drive Circuit

The stepper motor is digitally regulated by a controller unit sending pulses to the motor driver circuit [5]. Due to digital logic control problems appearing at moments such as start, stop, acceleration and deceleration, the design of the driver circuit is important when developing a stepper motor system. The controller can be applied as an application specific integrated circuit (ASIC), on a microprocessor or other logic integrated circuit (IC) [10]. The advantage of a microprocessor is the re-programmability, a quality that makes it slower in comparison to an ASIC, as this logic construction is optimised for the given application.

In the elaborated system the drive circuit act as a bridge between the controller and the actual motor. Within the driver circuit several modules are integrated, which are all resulting in a control of the winding current. Depending on the stepper motor, two different driver types are used. The drives are divided as bipolar and unipolar, and differs in the number of used windings and energisation sequence. The unipolar drive use four windings, each attached to a positive power supply which in turn is connected to a centre tap. Each winding is connected to ground by a switch, controlling the current flow from the centre tap through the windings in a given order making each winding being energised in turn. An example of the sequence of energising is illustrated in a timing diagram shown in Figure 2.8 where A, B, C and D are the separate windings i.e. the separate phases. The unipolar control ensures the rotor to move one position at a time and is advantageous in applications with a variance reluctance stepper motor due to the direction of the current not being relevant when creating the torque [3, 5].
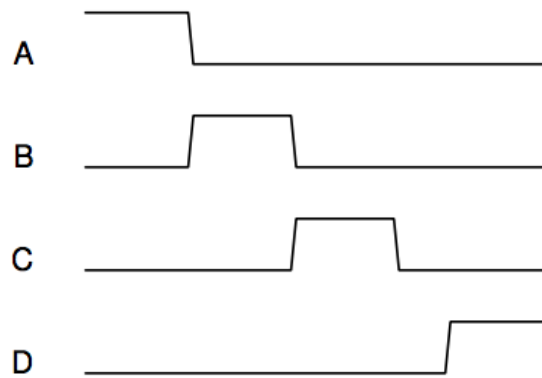
Figure 2.8: Timing diagram of a unipolar motor control sequence.

A bipolar two phase control is utilised by turning on and off switches in two H-bridges controlling the direction of the current flow in the motor windings. Figure 2.9 illustrates the A phase drive configuration where switch S1 and S4 as well as switch S2 and S3 work in pairs. When S1 and S4 are turned on the voltage and current through the winding inductance will be positive. With S2 and S3 turned on the voltage and current flow in the opposite direction. The switch pairs cannot be turned on at the same time, but by being off simultaneously the output current will reach zero. This is necessary as the inductance current can not change direction instantaneously and the stored energy in the inductance is dissipated through the diodes during off-time. Current is controlled by altering the voltage on the windings though Pulse Width Modulation, PWM.
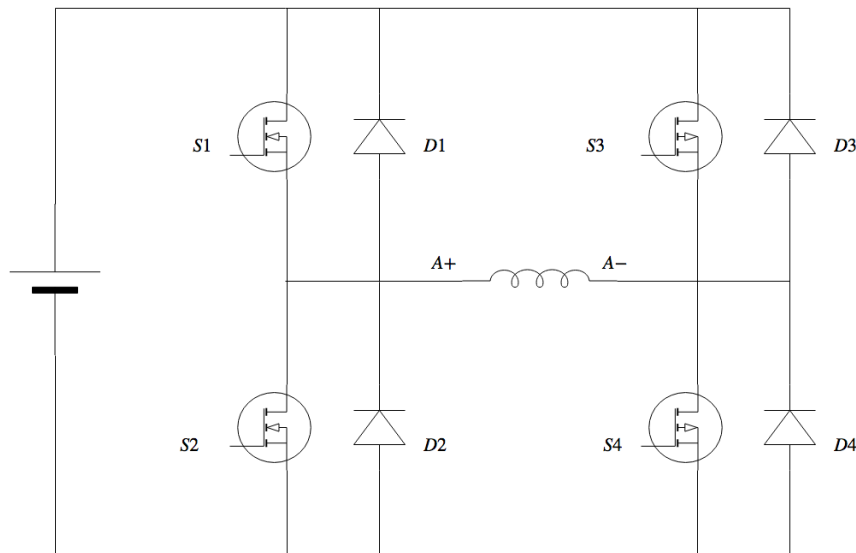
Figure 2.9: A phase generated from H-bridge in the driver circuit.

The stepwise energisation of the two windings establish a timing diagram shown in Figure 2.10 where a high value indicates a positive current in the winding and a low value represents a negative phase current with full stepping driver

mode[10]. Due to the direction of the current the windings will be energised in a specific manner providing a four step rotation of the rotor. The bipolar drive is suitable for the hybrid stepper motor [5].
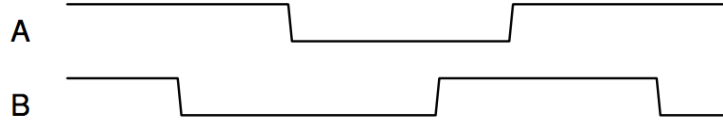
Figure 2.10: Timing diagram of a bipolar motor control sequence.

2.3 The Valve And Gearbox

The load of the valve control control system consist of a gearbox and valve and the torque from both components contributes to the load torque τ_l. The valve in this valve control system is a butterfly valve which open and closes by 90°. It has a compact design requiring a small installation space making it advantageous in space limited applications [13]. The gearbox is connected between the motor shaft and the load. It converts the motor torque and speed output to the high torque and low speed required by the valve, enabling the possibility of using smaller motor. Depending on the torque τ_e produced by the motor and the torque required by the valve τ_v the ratio between the two torques, the gear ratio n_G, is obtained as

$$\tau_v = n_G \tau_e \tag{2.16}$$

assuming a positive and constant gear rate [14].

The valve is used to control liquid flow. Its main components are the body, stem, and disc mounted as shown in Figure 2.11, provided by Johan Deger at LK Valves. Leakages are minimised as the disc closing tightly around the lining. Two components creates the total valve torque as

$$\tau_v = \tau_c + \tau_a, \tag{2.17}$$

where τ_c is the torque originating from construction and τ_a is the aerodynamic torque coefficient component. Construction torque τ_c depends on construction parameters such as friction and will increase with age [15, 16]. This is why having a motor able to produce more torque than nominally necessary is important, to count for increased construction torque and thereby extend the life time of the motor and valve system. The fluid flowing in the pipe applies pressure on the disk causing the second torque component. This additional aerodynamic valve torque depend on the disk angle and geometry of the nearby pipe. It is described by a normalised aerodynamic torque coefficient component τ_a. When the disk is closed and positioned at 0°, τ_a is generally small due to equal forces on both sides of the disk. Opening the disk increase the contribution from the fluid, changing τ_a. At 80° the aerodynamic valve torque reach its maximum value, corresponding to the position where the fluids in the pipe has the largest impact on the disk. In the end of the opening process, τ_a decrease to arrive at a small and balanced value at a fully opened disk at 90° [16, 17].

13
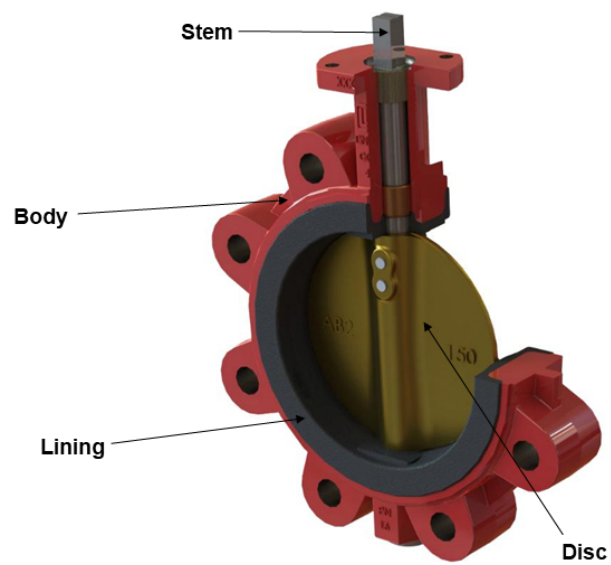
Figure 2.11: CAD model of the butterfly valve provided by Johan Deger at LK Valves.

3
Load Torque Estimation

Torque is the rotational analogue to force, measured in newton meter and translating Newtons second law $F = ma$ into

$$\tau = J\ddot{\theta} = J\frac{d\omega}{dt}, \tag{3.1}$$

where J is the body inertia equivalent the mass m and $\ddot{\theta}$ the angular acceleration equivalent the linear acceleration a. Superposition is utilised to measure a net torque, hence the total torque of a motor is described as (2.15), relating the produced electrical torque τ_e to the detent torque $\tau_d(\theta_e)$ and the load torque τ_l. Rewriting (2.15) results in

$$\tau_l = \tau_e - \tau_d(\theta_e) - J\frac{d\omega_m}{dt} - B\omega_m, \tag{3.2}$$

which additionally includes the viscous damping constant B [9]. This constant denotes for the friction and second order effects due to eddy currents and hysteresis in the motor [9]. Noticeably, the produced electromagnetic torque is equal to the sum of the applied load torque and the detent torque when the rotor speed is zero. With an assumption of a constant rotational speed, i.e. the stepping of the motor is smooth enough to be seen as uninterrupted reduce (3.2) to

$$\tau_l = \tau_e - \tau_d(\theta_e) - B\omega_m. \tag{3.3}$$

Estimating τ_l by evaluating the detent torque, loss component $B\omega_m$ and motor torque for the specific system enables the possibility to monitoring the valve health without the usage of a torque sensor. Both B and the detent torque are small components compared to the motor torque, why the latter is the main focus when trying to estimate τ_l.

3.1 2-Phase Stepper Motor Torque Expression

An expression regarding the torque produced by a 2-phase hybrid stepper motor is initiated using the rule of energy conservation in the coupling field. The same reasoning is applicable to a motor with more phases. For the 2-phased motor the differential form of the comprise

$$dW_e = dW_f + dW_m, \tag{3.4}$$

where dW_e is the electrical energy applied to the coupling field, dW_f the energy from electrical system reserved in the coupling field and the mechanical energy dW_m moving the rotor [5].

Dividing the electrical input energy dW_e in its fundamental components, it can be expressed as

$$dW_e = (e_A i_A + e_B i_B)dt, \tag{3.5}$$

where e_A and e_B are the induced EMF from a change in flux concerning each phase as shown in (2.10) and i_A and i_B are the respective phase currents [5].

The relation between mechanical energy and torque τ_e is described as as [5]

$$dW_m = \tau_e d\theta_m. \tag{3.6}$$

Fixing the rotor in a set position making $d\theta_m = 0$ and causing dW_m to be zero, entails (3.4) and (3.5) to merge in [5]

$$dW_f = dW_e = (e_A i_A + e_B i_B)dt. \tag{3.7}$$

Using (2.10) in (3.7) and integrating over the rotor angles, the total amount of energy stored in the coupling field is described as

$$W_f = \int_0^{\Psi_A} i_A d\Psi_A + \int_0^{\Psi_B} i_B d\Psi_B. \tag{3.8}$$

With the rotor rotating a small distance $d\theta_e$ together with an assumption of constant currents during this period, (3.4), (3.6) and (3.8) form

$$i_A d\Psi_A + i_B d\Psi_B = dW_e = dW_f + \tau_e d\theta_m. \tag{3.9}$$

With $d\theta_m$ approaching zero, (3.9) is reformulated, expressing the motor torque as

$$\tau_e = -\frac{\partial W_f}{\partial \theta_m} + i_A \frac{\partial \Psi_A}{\partial \theta_m} + i_B \frac{\partial \Psi_B}{\partial \theta_m} = \frac{\partial W_f'}{\partial \theta_m}, \tag{3.10}$$

where the latter term W_f' is the coenergy of the system. Coenergy is a concept not having a physical aspect, however being used to express electromagnetic force [18]. In a motor assumed not to reach saturation the energy, as a function of angular position and current, is linear in the magnetisation curve [5]. Coenergy resembles the energy stored in the coupled field and is expressed as

$$W_f' = \int_0^{i_A} \Psi_A di_A + \int_0^{i_B} \Psi_B di_B. \tag{3.11}$$

The flux linkage will then also be linear to the current as

$$\begin{aligned} \Psi_A &= L_A(\theta_e)i_A + \Psi_M cos(\theta_e) \\ \Psi_B &= L_B(\theta_e)i_B + \Psi_M sin(\theta_e), \end{aligned} \tag{3.12}$$

where $L_A(\theta_e)$ respectively $L_B(\theta_e)$ are the inductance of each phase depending on electrical angle θ_e [5]. Inserting (3.12) in (3.11) together with $\theta_e = N_r \cdot \theta_m$, then

(3.10) results in

$$
\tau_e = \underbrace{\frac{1}{2}i_A^2 \frac{\partial L_A(N_r\theta_m)}{\partial \theta_m} + \frac{1}{2}i_B^2 \frac{\partial L_B(N_r\theta_m)}{\partial \theta_m}}_{\text{Reluctance Torque}}
$$
$$
\underbrace{- N_r\Psi_M i_A sin(N_r\theta_m) + N_r\Psi_M i_A cos(N_r\theta_m)}_{\text{Permanent Magnet Torque}}, \tag{3.13}
$$

where the former segment of the equation is the contribution from the reluctance torque and the latter is the contribution from the permanent magnet.

As shown in (3.13) the contribution from the reluctance torque is depending on a rotor position dependent inductance. With aligned stator and rotor teeth the reluctance is low introducing a high flux at a given current, enabling a high inductance. At a misaligned position, the reluctance at a given current is higher resulting in a lower inductance. Due to the construction of the stator and rotor teeth, the inductance is approximately periodic with an average phase inductance L_0 and a rotor position dependent inductance variation L_1 [3]. Concerning the 2-phase stepper motor the A and B position dependent inductance are 180° misaligned from each other and expressed as

$$
\begin{aligned}
L_A(\theta_m) &= L_{0,A} + L_{1,A}sin(2N_r\theta_m) \\
L_B(\theta_m) &= L_{0,B} - L_{1,B}sin(2N_r\theta_m).
\end{aligned} \tag{3.14}
$$

Using (3.14) in (3.13) the torque expression for a 2-phase stepper motor is derived as
$$
\begin{aligned}
\tau_e = &\left(i_A^2 N_r L_{1,A}cos(2N_r\theta_m) - i_B^2 N_r L_{1,B}cos(2N_r\theta_m) \right) \\
&+ N_r\Psi_M \left(-i_A sin(N_r\theta_m) + i_B cos(N_r\theta_m) \right).
\end{aligned} \tag{3.15}
$$

3.2   Motor Torque Estimation Using Power

Another estimate of τ_e can be derived from output power and rotational speed as

$$
\tau_e = \frac{P_{\text{out}}}{\omega_m}. \tag{3.16}
$$

In a realistic model of the motor the system losses need to be accounted for, as they are present during operation. Thereby, the input power can be related to the output power as

$$
P_{\text{out}} = P_{\text{in}} - P_{\text{loss}}. \tag{3.17}
$$

Calculating the output power for a 2-phase stepper motor is executed using (2.12) and (2.13). Ignoring the saturation effect, leaves only a position variance [8]. The input power to a system is then used to extract the electrical torque of the stepper motor. Concerning phase A such an operation results in

$$
\begin{aligned}
P_{in,A} &= v_A i_A \\
&= Ri_A^2 + L_A(\theta_e)\frac{di_A}{dt}i_A + \omega_e \left(i_A^2 \frac{\partial L_A(\theta_e)}{\partial \theta_e} - i_A\Psi_M sin(\theta_e) \right),
\end{aligned} \tag{3.18}
$$

while phase B resulting in

$$
\begin{aligned}
P_{in,B} &= v_B i_B \\
&= R i_B^2 + L_B(\theta_e)\frac{di_B}{dt}i_B + \omega_e\left(i_B^2\frac{\partial L_B(\theta_e)}{\partial \theta_e} + i_B\Psi_M cos(\theta_e)\right).
\end{aligned} \tag{3.19}
$$

Combined, (3.18) and (3.19) is described as

$$
\begin{aligned}
P_{in,\text{2-phase}} &= P_{in_A} + P_{in,B} \\
&= R(i_A^2 + i_B^2) + L_A(\theta_e)\frac{di_A}{dt}i_A + L_B(\theta_e)\frac{di_B}{dt}i_B \\
&+ \omega_m N_r\left(i_A^2\frac{\partial L_A(\theta_e)}{\partial \theta_e} - i_A\Psi_M sin(\theta_e) + i_B^2\frac{\partial L_B(\theta_e)}{\partial \theta_e} + i_B\Psi_M cos(\theta_e)\right),
\end{aligned} \tag{3.20}
$$

with the the last term being P_{out} according to (3.17) using term identification. Identifying the motor torque component from (3.13) and rewriting (3.20) as (3.16) generates

$$
\begin{aligned}
P_{in,\text{2-phase}} &= P_{in_A} + P_{in,B} \\
&= R(i_A^2 + i_B^2) + L_A(\theta_e)\frac{di_A}{dt}i_A + L_B(\theta_e)\frac{di_B}{dt}i_B \\
&+ \omega_m\left(\tau_e + \frac{1}{2}i_A^2\frac{\partial L_A(\theta_e)}{\partial \theta_e} + \frac{1}{2}i_B^2\frac{\partial L_B(\theta_e)}{\partial \theta_e}\right).
\end{aligned} \tag{3.21}
$$

To describe the generated motor torque in terms of input power and losses, (3.21) result in

$$
\begin{aligned}
\tau_e &= \frac{1}{\omega_m}\left(P_{in,\text{2-phase}} - R(i_A^2 + i_B^2) - L_A(\theta_e)\frac{di_A}{dt}i_A - L_B(\theta_e)\frac{di_B}{dt}i_B\right) \\
&- \left(\frac{1}{2}i_A^2\frac{\partial L_A(\theta_e)}{\partial \theta_e} + \frac{1}{2}i_B^2\frac{\partial L_B(\theta_e)}{\partial \theta_e}\right),
\end{aligned} \tag{3.22}
$$

as an additional motor torque expression in comparison to (3.13), having both position and rotational speed dependencies. Due to (3.14), (3.23) the torque expression for a 2-phase stepper motor is written as

$$
\begin{aligned}
\tau_e &= \frac{1}{\omega_m}\left(P_{in,\text{2-phase}} - R(i_A^2 + i_B^2) - L_A(\theta_e)\frac{di_A}{dt}i_A - L_B(\theta_e)\frac{di_B}{dt}i_B\right) \\
&- \left(N_r i_A^2 L_{1,A}cos(2N_r\theta_m) - N_r i_B^2 L_{1,B}cos(2N_r\theta_m)\right).
\end{aligned} \tag{3.23}
$$

4

Motor and Measurement Setup

In this section the employed stepper motor is described together with measurement setups to determine different motor specific parameters.

4.1 Stepper Motor System In Thesis

The stepper motor under investigation is module PD60-4-1160 from Trinamic, comprising a controller, driver and motor. Specifications for the module are collected from datasheets with an summary of important parameters stated in Table 4.1 and a simplification of the module implementation with specific processors and motor shown in Figure 4.1 [19, 20, 21]. The implementation consists of the 2-phase bipolar hybrid stepper motor QSH6018-86-28-310 from Trinamic together with a controller unit, driver stage and the sensOstep™ magnetic encoder to detect step [22]. The controller unit is implemented with microcontroller ARM Cortex-M3, motion controller circuit TMC429, pre-driver circuit TMC262 and a TMCL-memory [21]. Dividing the controller design in subdivisions establish a possibility for the microcontroller to control three different stepper motors simultaneously [23]. A MOSFET drive circuit implemented with H-bridges transfer the required currents to the motor windings. Typically the applied phase voltage has a value of 12, 24 or 48 V although the motor can withstand a maximum value of 51 V [20]. With the number of rotor teeth being 50, each full step length is equal to 7.2°, corresponding to $\frac{1}{50}$ of one mechanical turn.

The motor controller unit enables each full step to be divided into 256 microsteps. It also has an implemented current control, spreadCycle™, which behavioural characteristics are based on the chopper principle [22]. The chopper regulate the current to match a reference current by adjusting the applied phase voltage, determining the current slope. Trinamics own coolStep™ function is additionally implemented, adapting the winding current level depending on the load to minimise the power consumption and place the module in energy saving mode when steady state operation is reached [22]. By controlling the power transmission the efficiency is maximised and heating problem decreases. Benefits arising from higher efficiency is more perceptible with an increased rotational speed. As the coolStep™ function require knowledge about the applied load torque the feature stallGuard2™ is integrated in the controller unit [22]. This function measure the back-EMF level and translate the result to a corresponding load torque value for the coolStep™ function. The feature is used to locate the load torque value both for the coolStep™ function and to monitor the load torque and thereby prevent motor failure due to overload. Another feature implemented a microPlayer™ which increase the smoothness in ro-
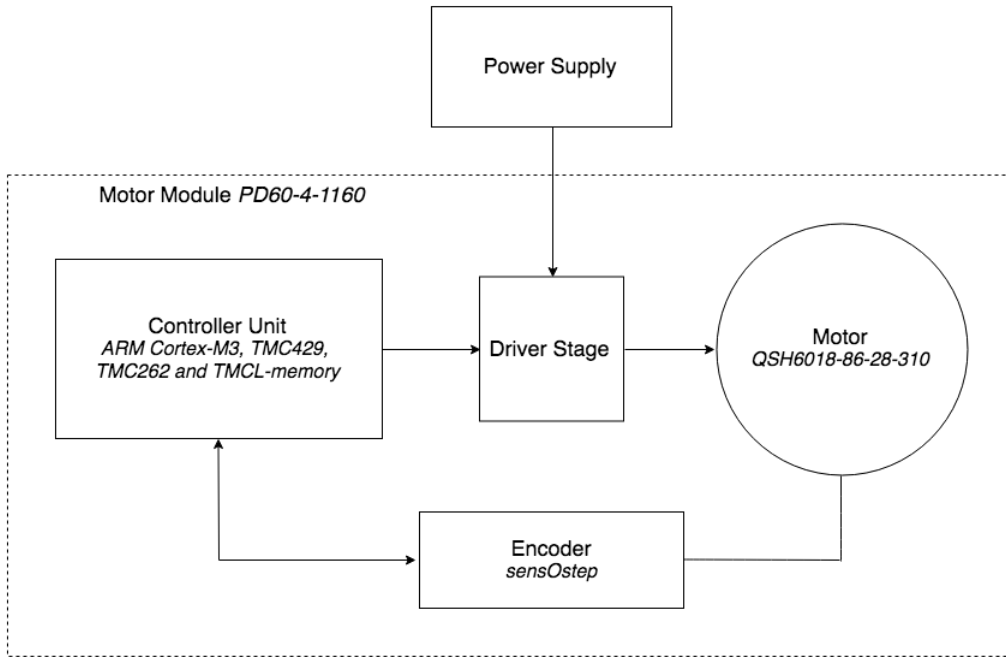
Figure 4.1: Simplified circuit description of motor module PD60-4-1160 with specifications stated in [21] and [20].

tation and enable microstepping [22]. Motor systems from Trinamic are operated using the combined protocol and programming language Trinamic Motion Control Language TMCL™. TMCL™ for motor applications is developed using a PC-based integrated development environment from Trinamic TMCL-IDE, connected to the motor through USB or field buses CAN, RS232 or RS485 [21]. Commands can be stored in the application and performed as stand-alone operation or be operated directly from a host. The TMCL-IDE furthermore offers a possibility to graphically monitor motor behaviour and parameters in real time. A large range of parameters can be altered to achieve an optimal application setting. However, in the project the standard values are considered and no fundamental characteristics have been changed.

The 2-phase bipolar hybrid stepper motor controls a butterfly valve from LK Valves with a holding torque of 250 Nm. According to Johan Deger at LK Valves, a gearbox with gear ratio 84:1 is used in the system to accomplish this torque. The gear box is supposed to be ideal, why the load torque of the system τ_l equals the torque acquired by the valve τ_v. Furthermore the gearbox should transfer a rotor speed of 21 rpm – 97 rpm to a valve speed of 0.3 rpm – 1.2 rpm with an actuation time of 13 – 60s. Due to the torque of the valve increasing with age, the motor should be able to deliver a torque to move a load requiring 300 Nm, having a safety margin of 20%.

Table 4.1: Specifications for Trinamic motor module PD60-4-1160 [19, 20].

Dimension	Nema24
#Rotor Teeth	50
Rated Current, i_{rms}	2.8 A
Peak Current, $i_{max_{peak}}$	4 A
Phase Voltage, v_{max}	51 V
Phase Voltage, v_{typ}	12, 24, 48 V
Holding Torque, τ_H	3.1 Nm
Phase Resistance at 20°, R	1.5Ω
Phase Inductance (typ.), L	6.8 mH
Rotor Inertia, J	840 g·cm^2

4.2 Motor Parameter Measurement Setup

Some parameters required for the theoretical model and torque estimators were not provided by the manufacturer and datasheet, whereas actual measurements on the real motor were necessary. Experiments and measurements were also conducted to verify the information and graphs provided by the datasheet.

4.2.1 Winding Resistance

In order to obtain an accurate model of the motor the winding resistance, seen in Figure 2.5, needs to be determined. This was done using a multimeter. The resistance measurement required the windings to be open circuited, as the measurement probes were connected according to Figure 4.2.
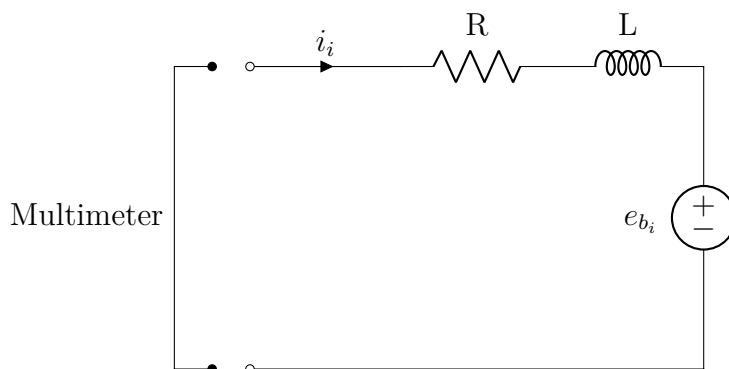
Figure 4.2: Measurement setup for winding resistance determination. The multimeter was connected to the open circuit winding.

4.2.2 Maximum Flux Linkage

To estimate the electrical torque given as (3.13) one of the motor specific parameters to determine is the maximum flux linkage Ψ_M. As $e = \frac{d\Psi}{dt}$, knowing the flux linkage from each phase from (3.12), the expressions for each phase induced voltage contribution are described as

$$
\begin{aligned}
e_A &= \frac{d\Psi_A}{dt} = L_A(\theta_e)\frac{di_A}{dt} + i_A\frac{\partial L(\theta_e)}{\partial \theta_e}\frac{\partial \theta_e}{\partial t} - \Psi_M\omega_m sin(\theta_e), \\
e_B &= \frac{d\Psi_B}{dt} = L_B(\theta_e)\frac{di_B}{dt} + i_B\frac{\partial L(\theta_e)}{\partial \theta_e}\frac{\partial \theta_e}{\partial t} + \Psi_M\omega_m cos(\theta_e).
\end{aligned}
\tag{4.1}
$$

Open circuit measurements result in zero current through the windings, establishing the induced voltage being equal to the input voltage, arriving in

$$
e_A = \frac{d\Psi_A}{dt} = -\Psi_M\omega_m sin(\theta_e),
\tag{4.2}
$$

$$
e_B = \frac{d\Psi_B}{dt} = \Psi_M\omega_m cos(\theta_e).
\tag{4.3}
$$

The induced voltage was created by rotating the motor shaft in a known and constant speed. By extracting the voltage curves over time using a digital oscilloscope, the mechanical speed was derived. Knowing the induced voltage over time the exact speed of the shaft rotation was established using the assumption of the induced voltage being two phase and offset by 90°. Such an estimation creates the opportunity of constructing the two phases as a complex voltage vector $V = V_A + jV_B$. The absolute of the created complex vector is the length of the vector and the amplitude of the induced voltage. The mean value of the vector during a set number of times will create a linear model whose slope is the frequency of the system. From this frequency the correct speed of the rotation was calculated and the value of Ψ_M determined.

4.2.3 Position Dependent Inductance

The rotor position dependent inductance was estimated applying the configurations shown in Figure 4.3. When conducting the experiment an external arm was attached perpendicular to the rotor shaft. As shown Figure 4.3 the arm had an equal length x on both sides of the shaft and an evenly distributed weight to minimise the impact on the rotor. Manual adjustment of the rotor angle was obtained by altering the position by y length units. With a measuring stick at a given length from the shaft, the rotational angle θ of the motor was with these lengths calculated using trigonometric identities.

The inductance values were extracted by connecting a LCR meter to the windings and measure the inductance at distinct rotor angles. The used equipment was an Atlas LCR model LCR40, with an accuracy of $\pm 1.5\%$ concerning inductance measurements [24]. In order to obtain conclusive results the experiment was done for both sides of the rotor, i.e. when the rotational movement was both clockwise and counter clockwise.
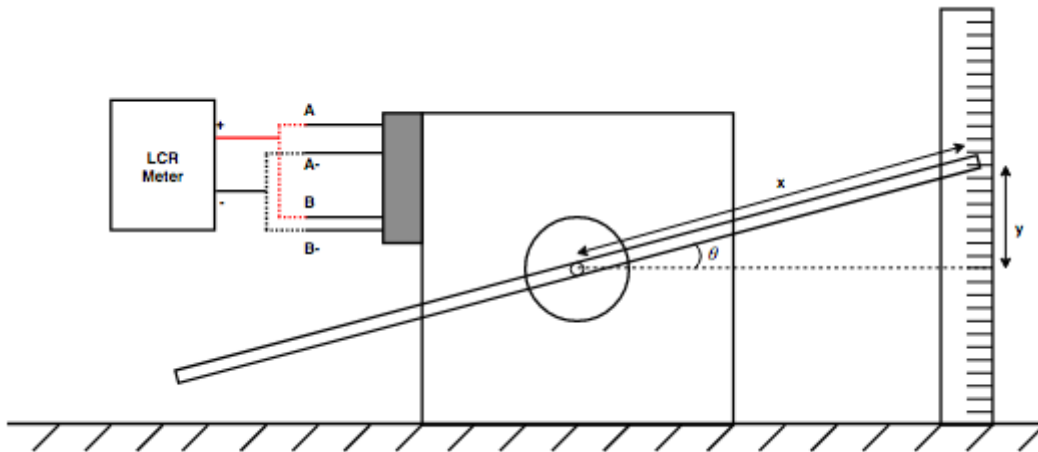
Figure 4.3: Setup of the position dependent inductance measurement.

4.3   Detent Torque Measurement Setup

In order to measure the detent torque the rotor was rotated by an external force. The motor was therefor disconnected from its digital control to ensure the measurements occurred without impact from other sources of force. To create a controlled rotation of the rotor an arm was placed perpendicular to the shaft. The procedure to extract the rotor angle θ_m were the same as to the measurements of the position dependent inductance in Section 4.2.3. At a given angular position the weight this rotational movement caused on the arm on the opposite side of the shaft was measured. The setup of the detent torque measurement is shown in Figure 4.4.
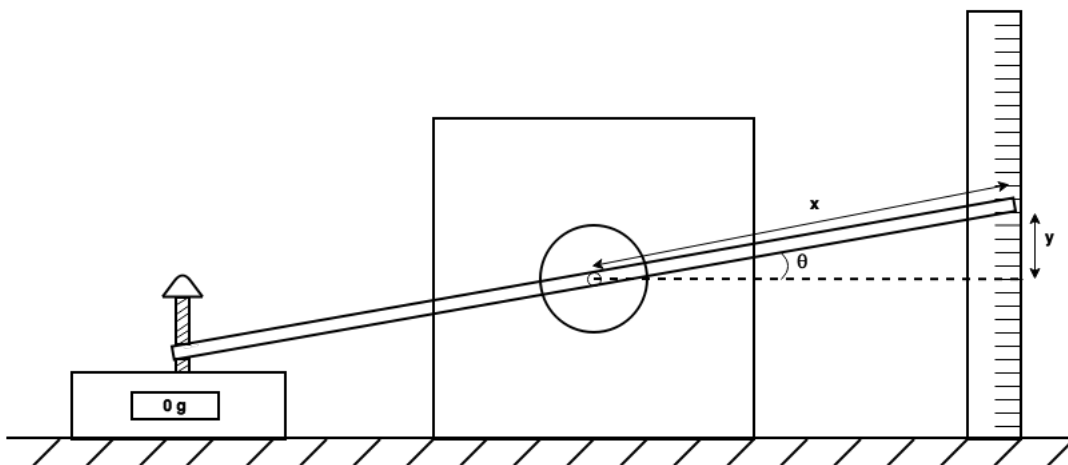
Figure 4.4: Setup for detent torque measurement.

Using the length l from the rotor centre to the point where the weight m was measured the torque on the shaft at a specific angular position is calculated as $\tau = m \cdot g \cdot l$ with g being the gravitational acceleration of 9.81 m/s². The sampling

frequency of the data, i.e. the data points analysed during the experiment, needs to fulfil the requirement of the specific motor being bipolar and having 2 phases together with one electrical turn being 7.2°. This translates into that for one electric period there must be at least two measurement points.

5

Extracted Stepper Motor Parameters

The following chapter contain results of performed motor measurements required to obtain a correct model of the system.

5.1 Motor Torque Measurements

5.1.1 Winding Resistance

The individual resistance of each winding was measured using a multimeter as illustrated in Figure 4.2. As a result, measurements concluded that both windings had a resistance value of 1.4 Ω.

5.1.2 Maximum Flux Linkage

Exposing the shaft of the investigated motor to a mechanical speed cause an induced voltage of each phase as shown in Figure 5.1. As assumed in Section 4.2.2 the two voltages are offset by 90° why the introduction of the complex voltage vector is accurate. Calculation of the complex voltage angle from such an estimation creates the model shown in Figure 5.2. Linearising this model results in the linear equation of $y = 1735x + 42.53$. From the slope of this straight line the mechanical speed of the system is determined as 324.67 rpm, a value close to the, by a tachometer, measured 331.2 rpm. Rearranging (4.1) to describe a cosine function with amplitude Ψ_m the flux linkages is additionally plotted in Figure 5.1. The maximum flux linkage Ψ_m is determined to be 0.8247 Wb.

5.1.3 Position Dependent Inductance

Measurements of the position dependent inductance resulted in the graph shown in Figure 5.3. Although some measured values are misplaced, the winding inductance can be mathematically described as a sine. Due to one electrical period being 7.2° and the bipolar drive of the investigated motor, two periods of the inductance variation are seen in the figure. The 180° shift of the measured phase inductance is explained by the 90° phase misalignment and the inductance position dependency provided in (3.14).

Presented in Table 5.1 are the key values extracted from the measurements such as the maximum, minimum and mean inductance values in addition to the
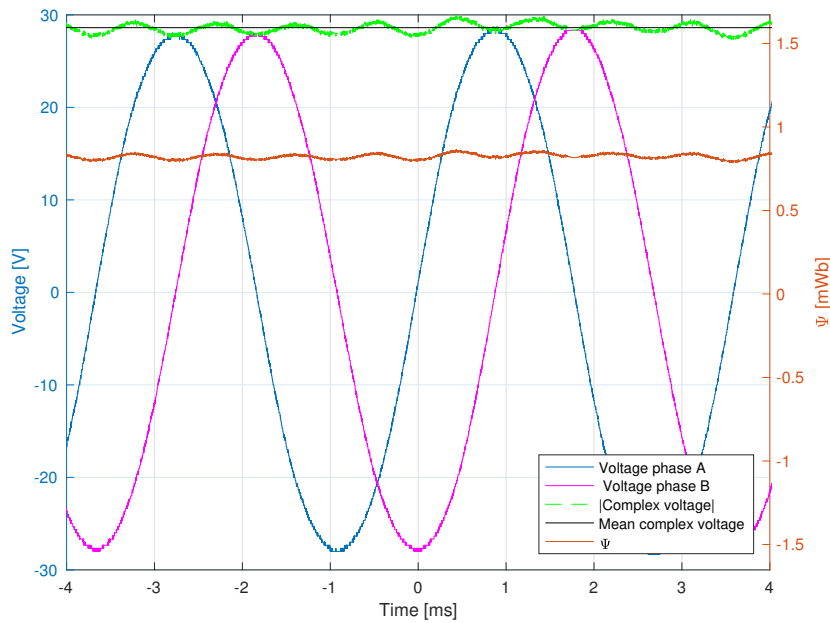
Figure 5.1: Induced voltages and their corresponding flux linkage values.
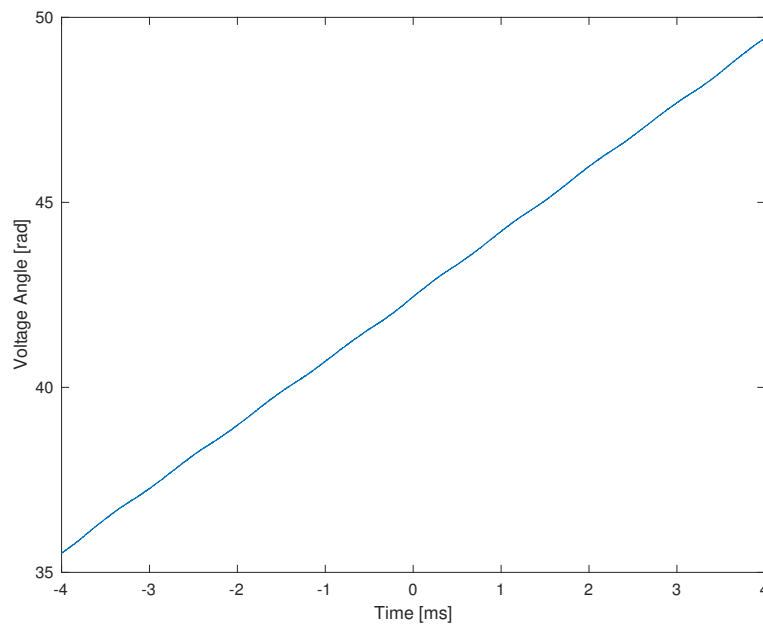
Figure 5.2: Model of approximate linear model resulting in a speed of 324.67 rpm.

largest inductance value deviation for both phases. With the individual phase inductance mean value differing by 15 µH, the total mean inductance for both phases is calculated as 6.4 mH. As the maximum deviation is 0.23 mH and 0.265 mH for phase A and B respectively, which is approximately 4% of the mean value, the inductance deviates with ±2% from the mean inductance value. Thereby, the inductance
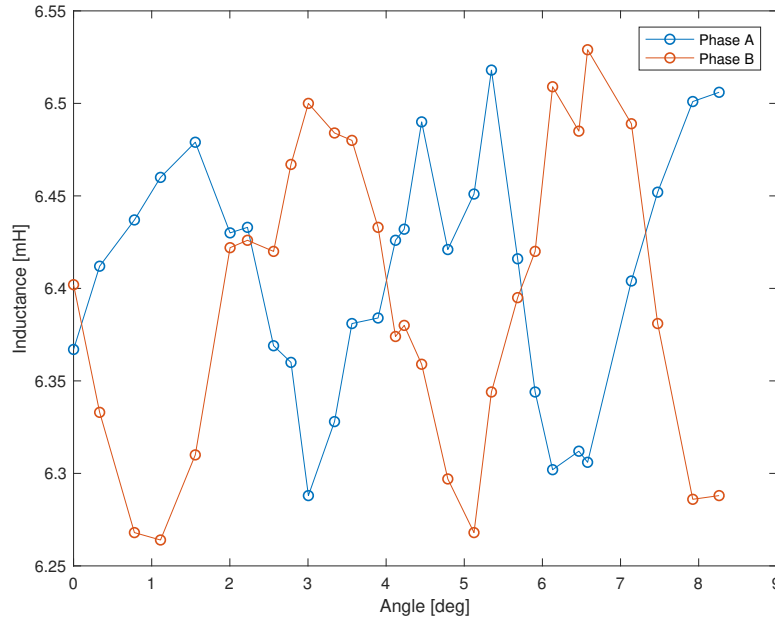
Figure 5.3: The figure shows the position dependent inductance for phase A and phase B.

is assumed to be constant and not position dependent.

Table 5.1: Result from position dependent inductance measurement.

	L_{max}	L_{min}	L_{mean}	$L_{\text{max deviation}}$
Phase A [mH]	6.518	6.288	6.408	0.23
Phase B [mH]	6.529	6.264	6.393	0.265

An explanation to the outlying data could be a result from the difficulty to establish a stable connection between the LCR meter probes and the winding circuit. The used equipment to measure the inductance was the Atlas LCR model LCR40 [24] with an accuracy of $\pm 1.5\%$ $\pm 1.6\mu H$, additionally explaining the edgy sine shape of the plot.

5.2 Detent Torque

Shown in Figure 5.4 are the measurement results of the investigated motor detent torque with the rotor rotating in both directions. As shown in the figure, the assumption of a periodical detent torque is correct and can additionally be mathematically described as a sine with an average amplitude of 0.09 Nm. The figure further present the four maxima within one electrical period occurring at 1.8°, 3.6°, 5.4° and 7.2°, a result of the four excitation steps of the bipolar 2-phase stepper motor to move the rotor teeth one period. As the detent torque should be zero during an alignment between the rotor and stator teeth, the illustration in Figure 5.4 is inaccurate. An

explanation to this result shown in Figure 5.4 could be a static torque component due to motor construction which needs to be applied to rotate the rotor. Consequently the result shows a combined static and detent torque. Figure 5.5 shows the detent torque without the static torque offset, resulting in amplitude of the position dependent detent torque determined to be 0.05 Nm.
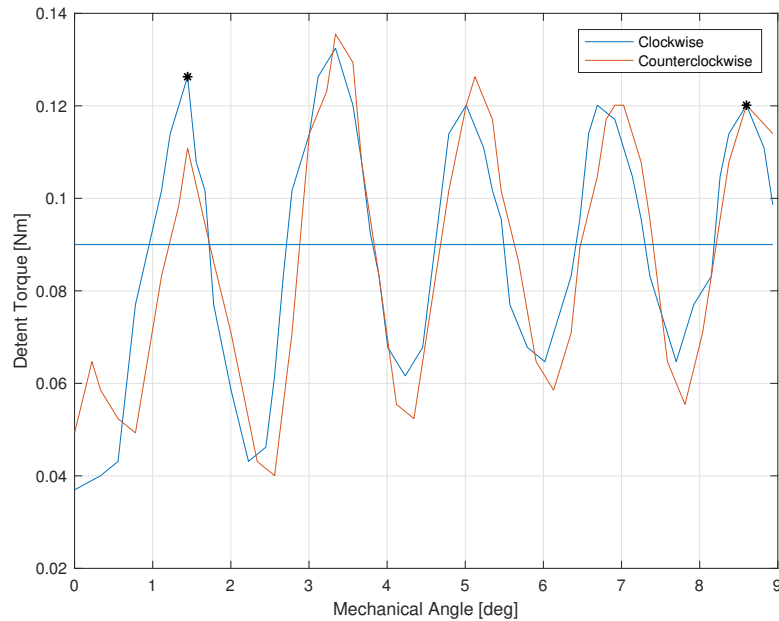
Figure 5.4: Position dependent result with static torque from detent torque measurement with rotor direction specified. The stars represent the outlines of one mechanical step, i.e. 7.2°.
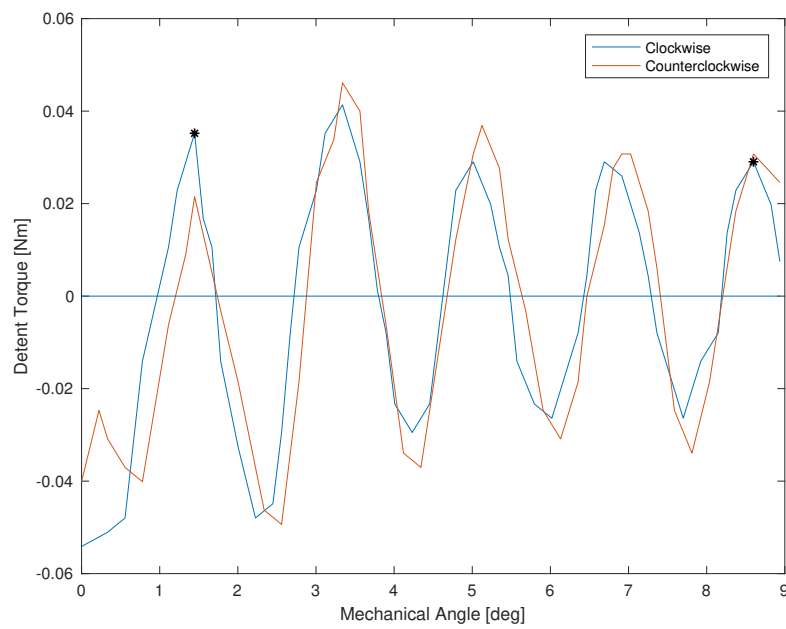
Figure 5.5: Position dependent without static torque result from detent torque measurement with rotor direction specified. The stars represent the outlines of one mechanical step, i.e. 7.2°.

6
Simulink Model

A model of the motor system was constructed using MATLAB Simulink. This section will elaborate on the Simulink model constellation of module PD-4-1160 from Trinamic.

6.1 Valve Control System model implementation

Using the extracted module PD-4-1160 parameters a valve control system model was created using Simulink. In the Simulink model, all torque components earlier denoted τ_i are changed to T_i, i being the system torque terms. An overview of the model setup is shown in Figure 6.1 where the calculation of motor torque τ_e, load torque τ_l, detent torque $\tau_d(\theta_e)$ and the valve systems mechanical dependency are represented with individual blocks and expressed by

$$J\frac{d\omega}{dt} = \tau_e - \tau_l - \tau_d(\theta_e) - B\omega_m, \tag{6.1}$$

which is a rearrangement of the relation presented in (3.2). As shown in Figure 6.1 the Load Torque block is a stand-alone component of the valve control system and is thus not dependent on the remaining blocks. Mechanical speed and position are calculated in the Mechanical System block and are required in order to generate τ_e in the Motor block as well as the torque contribution from the Detent Torque block.

6.1.1 Motor Block

A close-up of the Motor block is shown in Figure 6.2. A reference current is applied to the system, followed by a Driver and Current Controller block where a phase voltage is constructed by comparing the real current to the reference current. By applying the winding characteristics and the constructed phase voltage, the block representing Electrical Motor Component determine the real phase currents. The real phase currents are used in a closed loop as both an input to the Driver block as well as input to the electric torque calculation within the Mechanical Motor Component block. As seen in Figure 6.2, both the mechanical speed and electrical position are required input variables.

    Shown in Figure 6.3 is the close-up of the Current Reference block which produces reference currents i_A_ref and i_B_ref. The currents are designed as sine shaped signals with 90° phase shift. By applying an electric speed reference and a current amplitude i_amp_ref, the system is controlled. To minimise oscillations
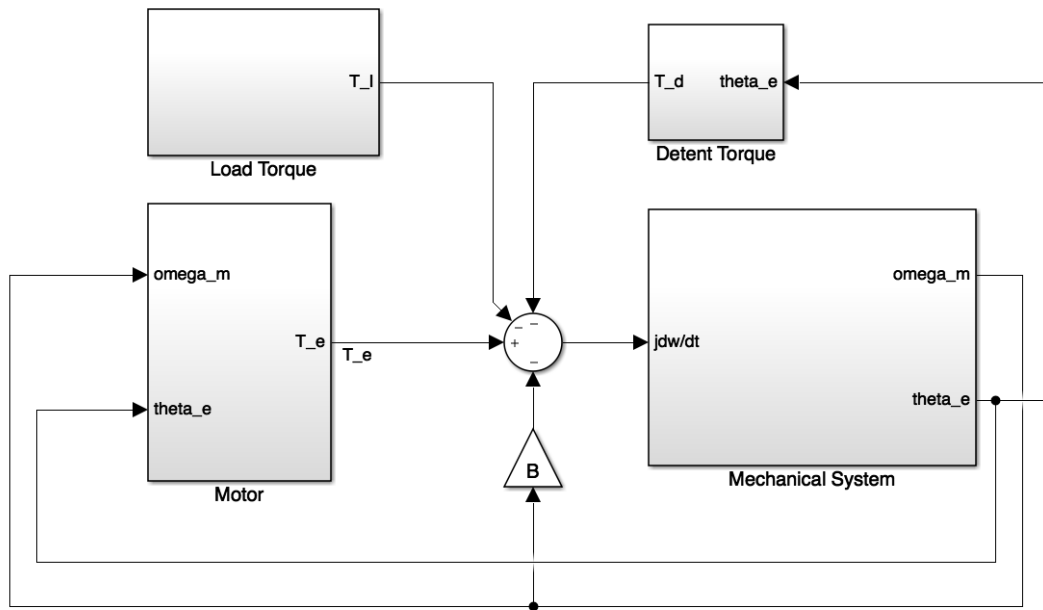
Figure 6.1: An overview of the Valve Control System model implemented in Simulink.

the speed reference *omega_e_ref* is created using a ramping step function with a reference frequency. Based on the desired electrical speed the reference frequency is chosen. The created reference speed *omega_e_ref* is integrated to access the electrical position *theta_e_ref*. Euler's formula is used to compose its exponential complex function. After multiplication with a reference current amplitude *i_amp_ref*, the exponential complex function real and imaginary components are extracted to express the reference currents *i_A_ref* and *i_B_ref* as sine and cosine wave forms.

Signals *i_A_ref* and *i_B_ref* are the input variables to respective phase Driver and Current Controller block illustrated in Figure 6.4. The figure only shows the build up for the Driver and Current Controller block for phase A as the block for phase B is identical. Within this block each current reference is compared to its corresponding real phase winding current. The current difference act as an input to the relay block in which the input is compared to the value 0.05 and -0.05, representing the width of the hysteresis band. If the reference current is 0.05 A larger than the real phase current, indicating that the real phase current should increase, the relay output is 1. For a reference current 0.05 A smaller than the real phase current, the relay output is set to 0. As the function of the Driver and Current Controller block is to create a phase voltage, the output from the relay, either 1 or 0, act as an input to the switch block. In the switch block the relay output is compared to the value 0.1. If the relay output is larger than 0.1, i.e. 1, a positive voltage *V_pos* will be applied as winding voltage and vice versa, creating a PWM voltage with a magnitude of either *V_pos* or *V_neg*.

The resulting voltage from Figure 6.4 act as an input to the block Electrical
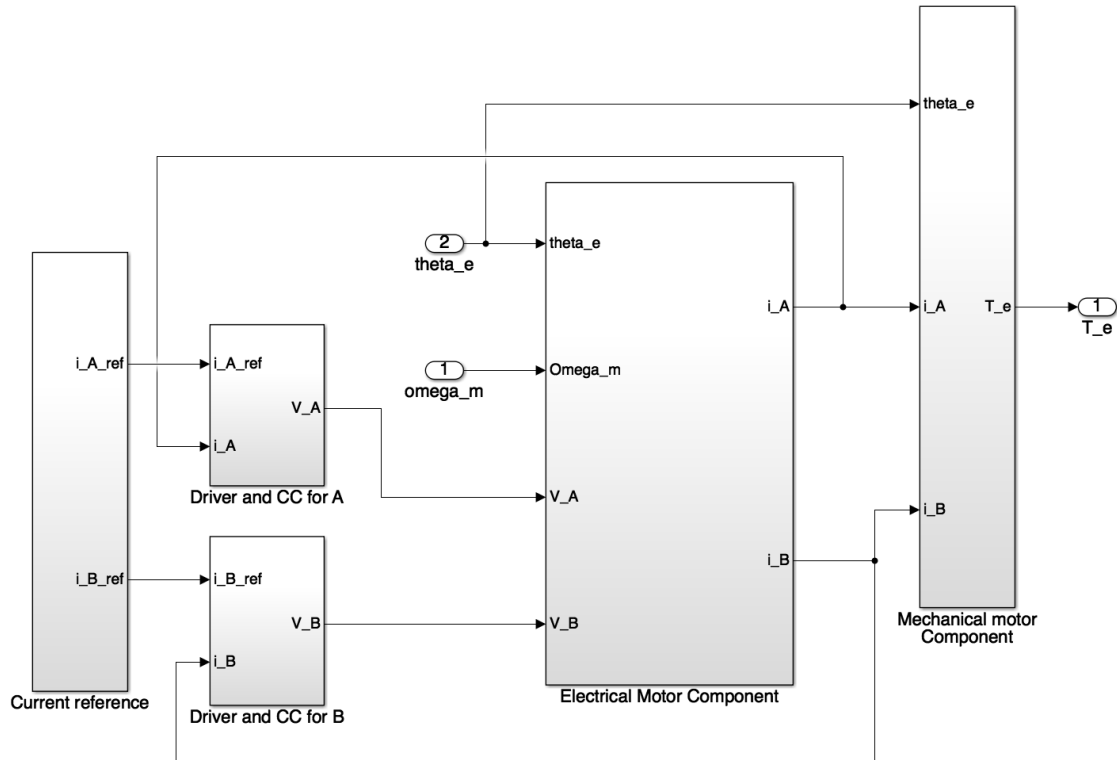
Figure 6.2: Motor block calculating the produced motor torque with individual blocks determining the reference current, motor driver and current controller, the motor electrical part and the mechanical motor characteristics.
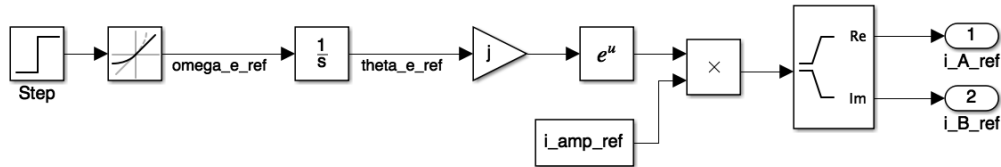
Figure 6.3: Current Reference block producing reference currents.

Motor Component. Other input variables to the block Electrical Motor Component are the mechanical speed *omega_m* and electrical position *theta_e*. A deconstruction of the block is shown in Figure 6.5 where the design of the block is derived from (2.12) and (2.13). Measurements on the stepper motor conducted the position dependent inductance to be negligible, reducing (2.12) and (2.13) to

$$
\begin{aligned}
v_A &= Ri_A + L_A \frac{di_A}{dt} - \Psi_M \omega_e sin(\theta_e), \\
v_B &= Ri_B + L_B \frac{di_B}{dt} + \Psi_M \omega_e cos(\theta_e).
\end{aligned}
\tag{6.2}
$$

Noticeable in Figure 6.5 is the usage of *omega_m* instead of *omega_e* as stated in the equation. The reason is that the flux component *Psi_m* was measured based
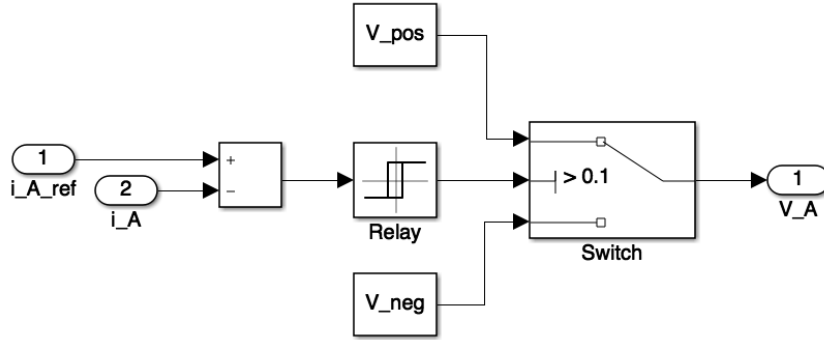
Figure 6.4: Hysteresis Regulator block, exemplified with phase A, creating a phase voltage depending on the difference between the reference and real phase current.

on the mechanical speed, hence a factor of N_r is already implemented in that term. The position dependent terms for each phase in (6.2) is the induced back-EMF earlier denoted as e_{b_i} and seen in Figure 2.5. Applying Laplace transformation to the equation result in

$$
\begin{aligned}
v_A &= Ri_A + sL_Ai_A - \Psi_M\omega_e sin(\theta_e) \rightarrow v_A + \Psi_m\omega_e sin(\theta_e) = i_A(R + sL_A), \\
v_B &= Ri_B + sL_Bi_B + \Psi_M\omega_e cos(\theta_e) \rightarrow v_B - \Psi_m\omega_e cos(\theta_e) = i_B(R + sL_A),
\end{aligned}
\tag{6.3}
$$

as presented in Figure 6.5. The output consist of the real winding current i_A and i_B.
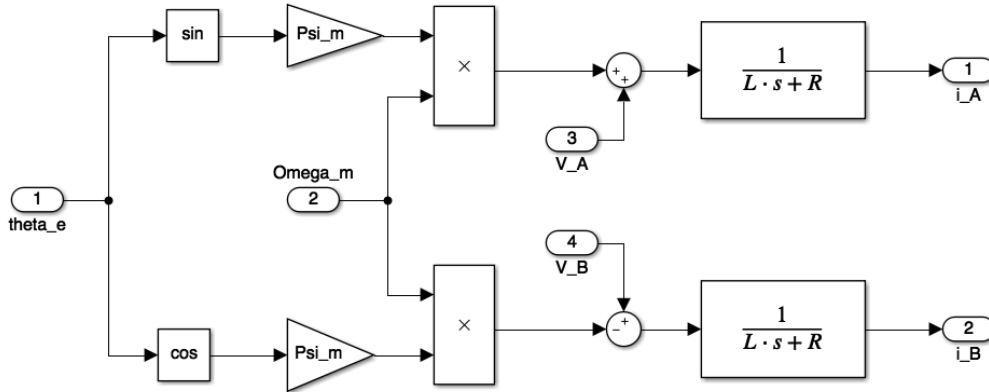
Figure 6.5: Electrical Motor block resulting in phase currents i_A and i_B.

Shown in Figure 6.6 is the close-up of the Mechanical Motor Component block constructing motor torque τ_e. Due to the negligible position dependent inductance (3.15) is reduced to

$$
\tau_e = N_r\Psi_M\left(-i_A sin(N_r\theta_m) + i_B cos(N_r\theta_m)\right).
\tag{6.4}
$$

By applying the same reasoning as for the Electrical Motor Component equation, N_r in (6.4) is neglected when constructing the model in Simulink. This because the

measured flux component is based on the mechanical speed and not the electrical speed.
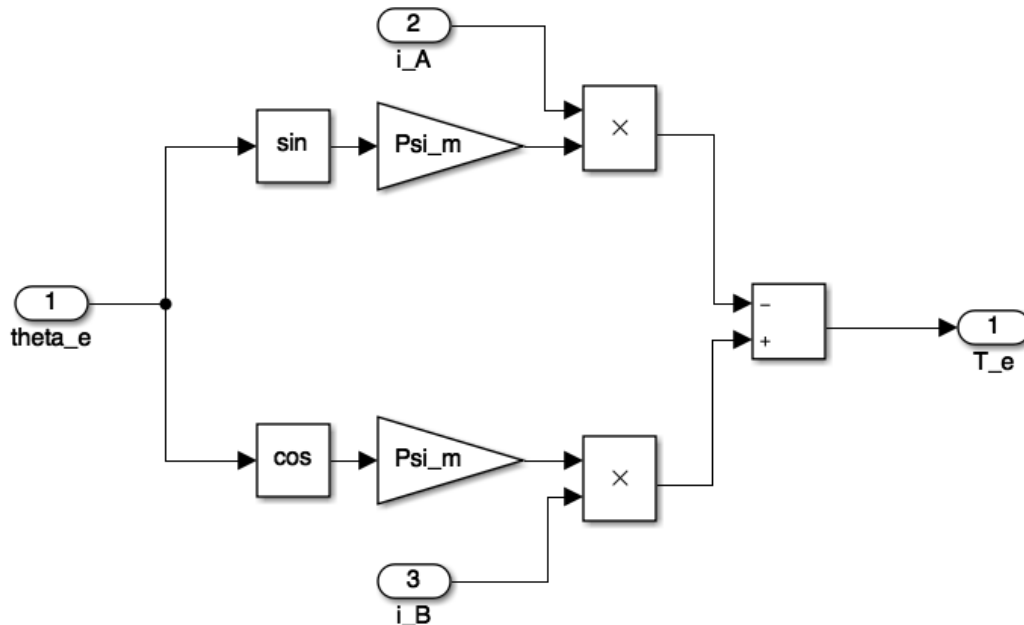
Figure 6.6: Mechanical Motor Component block which calculates the electrical torque produced by the motor using the real phase current, the electrical position of the rotor and the maximum flux linkage using (6.4).

6.1.2 Mechanical System Block

In the Mechanical System block seen in Figure 6.1 the angular speed and position of the rotor is derived as described by (6.1), whereas the block components are shown in Figure 6.7. By dividing the input variable with the rotor inertia J, the derivative of the mechanical speed is obtained. An integration block is applied, creating the mechanical speed. Thereafter the mechanical rotor position is created using an additional integration block. Multiplying the mechanical speed by the number of rotor teeth determine the electrical speed and thereby the electrical position can be obtained using an integration block. Shown in Figure 6.7 is a modification block and a *2*pi* constant, which result in a electrical position value ranging from 0 to 2π. Both the mechanical speed and electrical position are used as input variables in the Motor block. In addition, the mechanical speed is multiplied with the viscous damping constant B creating the term $B\omega_m$ described in (6.1) and seen in Figure 6.1.
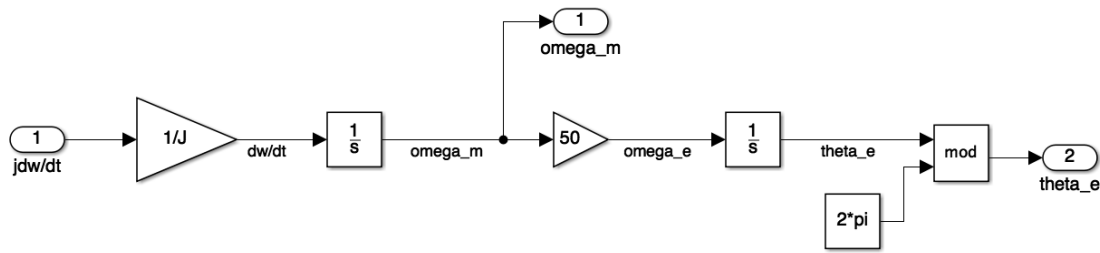
Figure 6.7: Mechanical System block where the system input $J\frac{d\omega}{dt}$ is used to determine the mechanical speed, mechanical position, electrical speed and electrical position.

6.1.3 Detent Torque Block

The Simulink model of the detent torque is based on (2.14) with parameter values extracted from motor measurements to produce a sinusoidal detent torque with four maximum during one electrical period. The implemented model of the detent torque is seen in Figure 6.8 where the electrical position act as an input variable. In the figure, an initial detent torque value *T_d0* is defined and set to the static torque seen in Figure 5.4. Thereafter, the sum of the components are multiplied by 4 due to the relation in (2.14). A sine curve is formed with an amplitude of *detent_amp*, resulting in the output variable *T_d*.
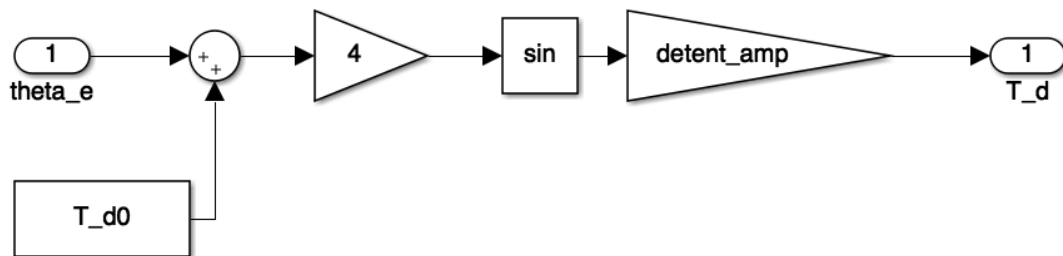
Figure 6.8: Detent Torque Block creating a sinusoidal torque component with four maximas during one electrical period.

6.1.4 Load Torque Block

The total torque τ_v of the butterfly valve consist of the aerodynamic torque component τ_a and a construction torque component τ_c as described in Section 2.3. Assuming an ideal gearbox the load torque of the system equals the valve torque as $\tau_l = \tau_v$. The construction of the load torque is shown in Figure 6.9 where τ_a is simplified as a triangular wave. As the load torque shape and magnitude depend on the valve position, the mechanical position act as an input variable, shaping the component T_a. By applying a constant T_c an offset value can be implemented in the Simulink model.
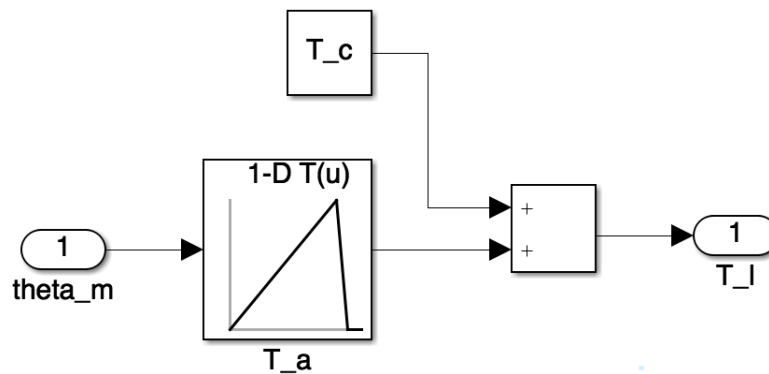
Figure 6.9: Load Torque Block creating the aerodynamic torque component as a triangular wave whose vertical offset is determined by the contruction torque component.

7

Simulation Results

Estimation mehods of the load torque τ_l in the valve control system are compared based on the system employed in the Simulink model described in Chapter 6. Determining motor torque τ_e is a necessity when estimating τ_l and in the Simulink model τ_e is generated by electrically modelling the motor as described by (3.15). Motor measurements determined the position dependent inductance to be negligable, simplifying (3.15) to (6.4) and reproduced as τ_e^1 according to

$$\tau_e^1 = N_r \Psi_M \left(-i_A sin(N_r \theta_m) + i_B cos(N_r \theta_m) \right). \tag{7.1}$$

Another approach of calculating τ_e is derived from (3.16) together with (3.17) using the output power and mechanical speed to describe the motor torque. For a 2-phase hybrid stepper motor (3.16) is expressed as (3.23). Due to the position dependent inductance being neglected, (3.23) is re-formulated and denoted τ_e^2 as

$$\tau_e^2 = \frac{V_A i_A + V_B i_B - (R_A i_A^2 + R_B i_B^2)}{\omega_m}. \tag{7.2}$$

In each section the used parameters for the specific simulation are specified. These parameters act as input values to the Simulink model and denotes the reference values to the controller in an implementation. Simulation sequences corresponding to signals measured by sensors in an implementation such as V_A, V_B, i_A, i_B and ω_m, have been derived based on the two last simulated periods. The average of these values are used when calculating τ_e^2. Concerning τ_e^1, its value is derived calculating the mean of (7.2) during the two last simulated periods, rather than calculating (7.2) using the mean of the individual parameters. The value of B is not known in this thesis. Thereby an assumption of it having a 5% impact during operation with a mechanical speed of 400 rpm was made, i.e. $B = 0.0024$ Nms/rad.

7.1 Verification Of Model Motor Torque Estimation

The Simulink model is built to mimic Trinamic module PD60-4-1160. In the model, τ_e^1 is utilised to describe the mechanical motor behaviour. Verification of the Simulink model is executed by comparing maximum motor specific torque versus velocity curves generated by Trinamic, accessible in the hardware datasheet [20] for module PD60-4-1160. A specification of the used parameters in the simulation are defined in Table 7.1. The stepper motor controlling the valve is supposed to operate in a

range of 21 rpm – 97 rpm, resulting in the full speed range provided by Trinamic not being evaluated. Instead the tests were performed in the mechanical speed range of 20 rpm – 200 rpm to demonstrate the curve shape trends.

The verification was executed by varying the mechanical speed and observing the maximum applied load torque before reaching instability. In order to detect system instabilities a curve defining the difference between the electrical reference angle and the real electrical rotor angle was established. As the motor is described as a microstepping synchronous motor, the applied winding current lead the real rotor angle and thereby cause a rotation. System instability indicates an angle difference of 90°. Instability was noted when the rotor speed became high and negative, indicating a loss of rotor and stator synchronism. By successively increasing τ_l the system was forced in to instability, enabling observation of at which torque the instability occurs. Observations were thereafter compared to the torque curve provided by the PD60-4-1160 datasheet [20], where an increase in torque for low speeds, reaching a top value of approximately 2.7 Nm at 50 rpm can be noted. The top is followed by a decrease in torque where the value reach 1.5 Nm at 200 rpm and 0.8 Nm at 400 rpm.

Table 7.1: Parameter settings for simulation verifying the Simulink model motor torque estimation being equal to the torque curve provided by Trinamic.

V_{in}	24 V
$I_{in,rms}$	2.8 A
R	1.4Ω
ω_m	20 rpm – 200 rpm
$\tau_{l,app}$	10 Nm
B	0.0024 Nms/rad

The results from the Simulink simulations are shown in Figure 7.1. It satisfactorily indicates the motor to manage a load over 2.5 Nm up to 100 rpm comparable to the result in the datasheet for module PD60-4-1160 [20]. Comparing the torques during the period 100 rpm – 200 rpm, the simulation results in a different maximum torque than defined by Trinamic. However, due to the low resolution in the figure in the datasheet for module PD60-4-1160 [20], the supposed torque at a given speed is difficult to extract and the result rather demonstrates a satisfying trend verification.
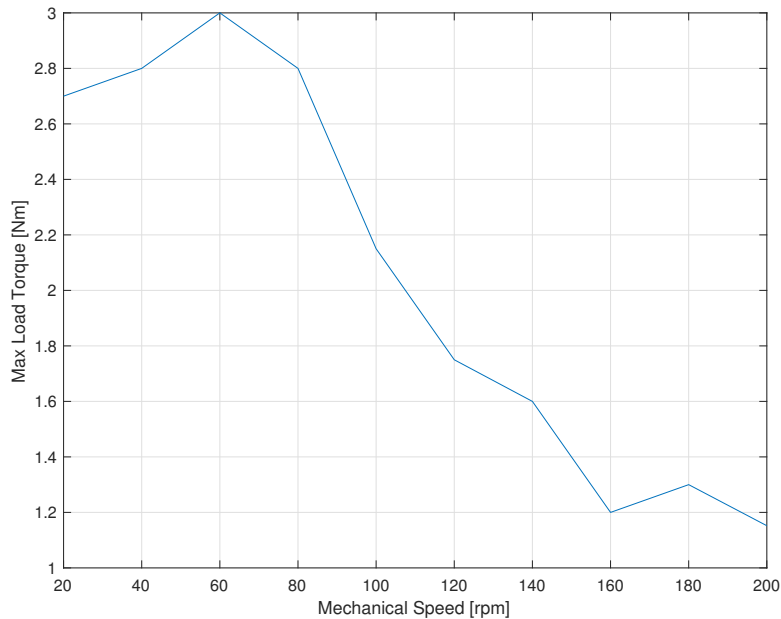
Figure 7.1: Results from Simulink simulations with different rotational speeds and their corresponding maximum allowed torque values.

7.2 Comparison Of Motor Torque Equations

As the two methods of calculating τ_e require different sensors when implemented, a comparison of the two is important in order to draw the conclusion of the most suitable approach when estimating τ_l. Different settings and simulated sensor noise has been generated in order to provide a comparison of necessary sensor resolution between τ_e^1 and τ_e^2. Measurement uncertainties affect all necessary extracted parameters e.g. currents and voltages. However, in the following simulations uncertainties concerning resistance and speed when calculating τ_e^2 together with position and Ψ_M when estimating τ_e^1 are the only considered.

7.2.1 Supply Voltage And Speed Variation

One aspect of evaluation when comparing the torque algorithms are the affects of different input voltages. With parameter settings defined in Table 7.2, two results were generated varying the mechanical speed for a supply voltage of 24 V respective 48 V.

Figure 7.2 shows the estimated motor torques τ_e^1 and τ_e^2 and the total load torque $\tau_{l,app} + B\omega_m$ during operation with a supply voltage of 24 V. The relation between the estimates and the total load torque during 24 V input voltage operation is shown in Figure 7.3. Increasing the supply voltage to 48 V results in the τ_e^1, τ_e^2 and a total load torque as shown in Figure 7.4. The relation between the estimates and the total load torque as for the 24 V case was done for 48 V operation and the results are presented in Figure 7.5.

Table 7.2: Parameter setting for simulation measurement comparing motor torque algorithms for two separate supply voltages and speed variations.

V_{in}	24 V & 48 V
$I_{in,rms}$	2.8 A
R	1.4 Ω
ω_m	20 rpm – 200 rpm
$\tau_{l,app}$	1 Nm
B	0.0024 Nms/rad
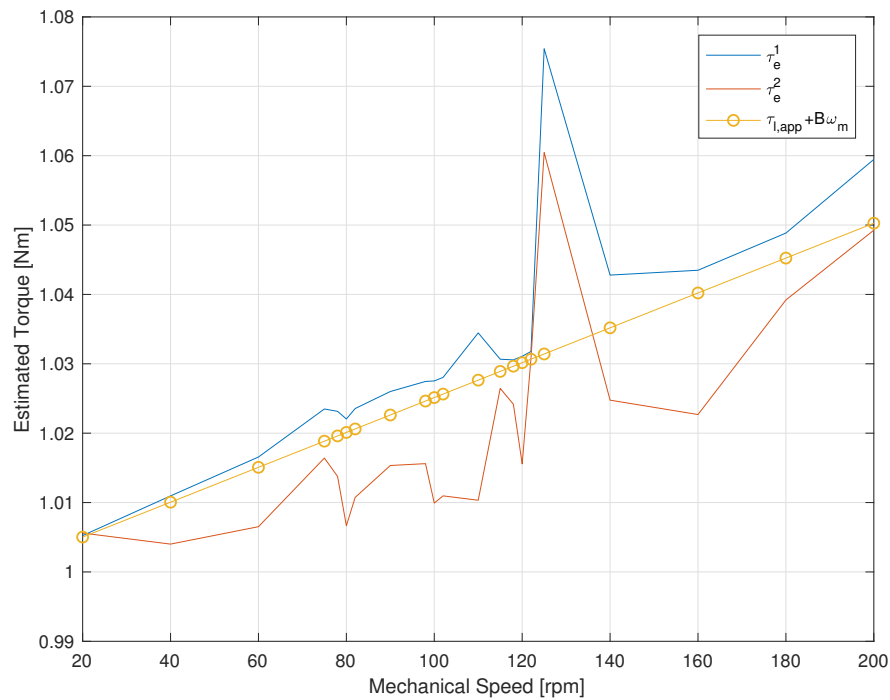
Figure 7.2: Comparison of τ_e^1, τ_e^2 and the total load torque with a supply voltage of 24 V during different operational speeds.
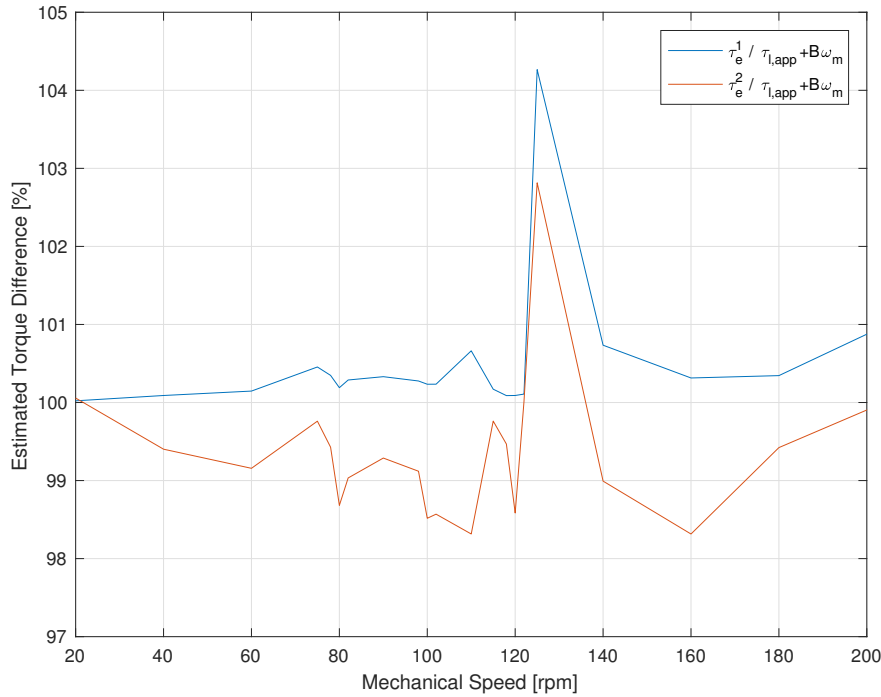
Figure 7.3: Relation in percentage between calculations of τ_e^1 and τ_e^2 with a supply voltage of 24 V during different operational speeds.

Shown in Figure 7.2 and Figure 7.4 are the increase in generated motor torque for respective supply voltage when increasing the mechanical speed. This is expected due to the speed dependent term comprised as Bω. The curve representing the total load torque is linearly increasing in both cases, whereas there is a slight variation in τ_e^1 and τ_e^2 increment. As seen in Figure 7.2 and Figure 7.4, spikes occur in the same applied speeds for both estimates, which are 125 rpm for 24 V input voltage and 100 rpm at 48 V voltage operation. These values are a result of system resonance, a problem occurring in the real motor during certain speeds due to characteristics of motor system and the load [2, 3]. The following simulations requiring a constant speed will avoid these resonances. By considering the operational range provided by LK Valves, a mechanical speed of 90 rpm is chosen for these simulations.

Further, the difference between the total load torque and the estimates are depicted in Figure 7.3 and Figure 7.5. By comparing the figures concludes that the differences are low. Including the spikes the maximum deviations are during 24 V 4.2% and 2.8% for τ_e^1 respective τ_e^2 and 0.9% and 2.8% for τ_e^1 respective τ_e^2 during 48 V. Neglecting the spikes, the maximum deviation shown in Figure 7.3 are 0.9% respective 1.7% for τ_e^1 and τ_e^2. For operation with 48 V supply voltage the maximum difference in percentage is 0.9% for τ_e^1 and 1.1% for τ_e^2. Ideally τ_e^1 and $\tau_{l,app} + B\omega_m$ would be equal but due to the low motor inertia the curves deviates from this assumption. Applying a low inertia result in the mechanical speed oscillating in steady state, making the average detent torque not zero, causing a torque difference between the estimated τ_e^1 and the correct torque $\tau_{l,app} + B\omega_m$.

43
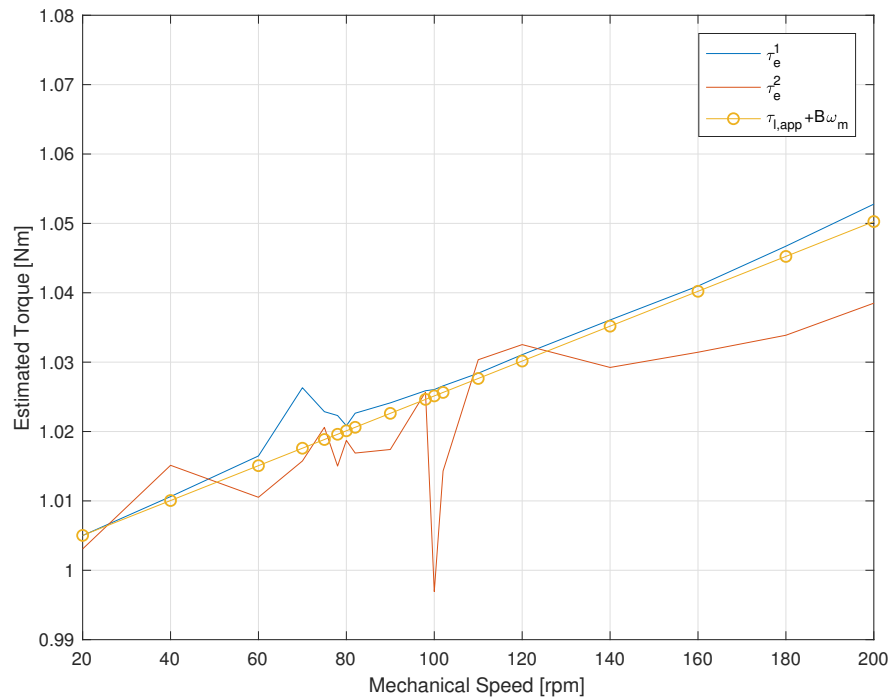
Figure 7.4: Comparison of τ_e^1, τ_e^2 and the total load torque with a supply voltage of 48 V during different operational speeds.

Even so, the maximum difference is, neglecting the resonance frequencies, under 1% and thereby the assumption of equality is acceptable.

Conclusions can be drawn that an increase in supply voltage will lower the difference in percentage between the generated motor torque and the estimates, making the estimates more accurate. This is however not unexpected as the system is controlled using PWM and a higher voltage level would result in a better current control and thereby a more adjustable system.
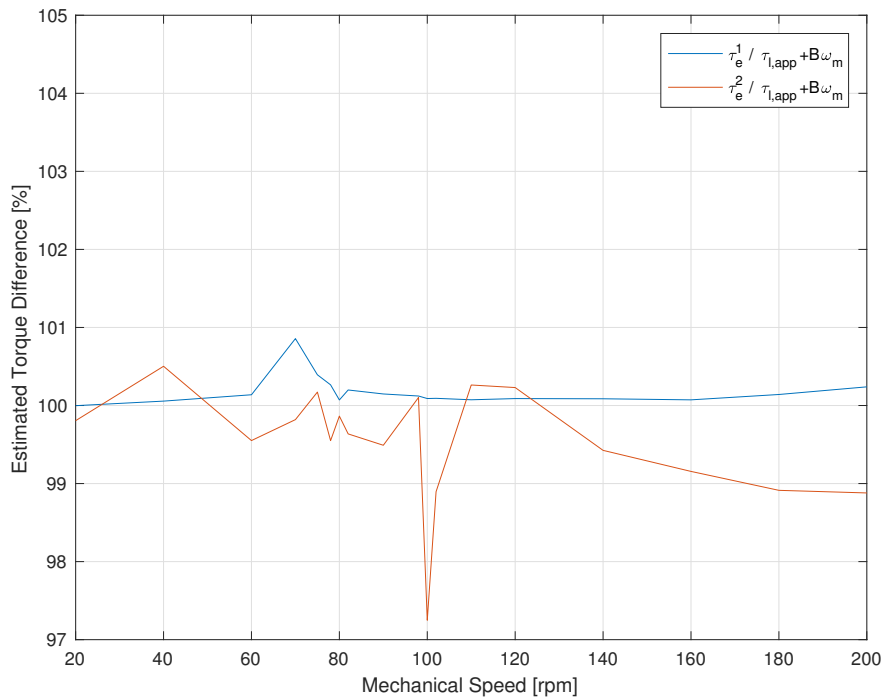
Figure 7.5: Relation in percentage between calculations of τ_e with a supply voltage of 48 V during different operational speeds.

7.2.2 Resistance Variation

A comparison between the two motor torque algorithms was performed with respect to variations in resistance value in the model and in the estimator τ_e^2. An increase in temperature in the motor windings will increase the resistance value, which will have direct impact when calculating power losses required in τ_e^2 according to (7.2) and indirect affecting the estimate τ_e^1. Two tests were executed where the first one regarded a variation of winding resistance of the Simulink model and the calculation of τ_e^2. The second test estimated the motor torque deviation of τ_e^2 using a resistance value unequal to the winding resistance in the Simulink model. The resulting mean values of the individual estimates from the first test are shown in Figure 7.6. During the simulation the parameters described in Table 7.3 were used.

Table 7.3: Parameter setting for simulation measurement comparing motor torque algorithms for resistance variation.

V_{in}	48 V
$I_{in,rms}$	2.8 A
R	$1\,\Omega - 2\,\Omega$
ω_m	90 rpm
$\tau_{l,app}$	1 Nm
B	0.0024 Nms/rad
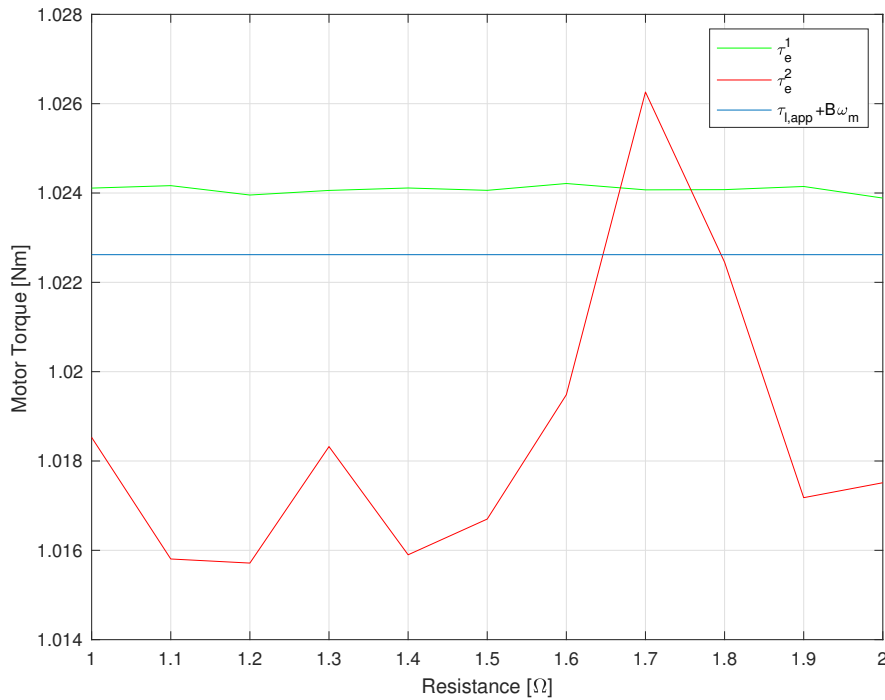
Figure 7.6: Comparison of τ_e^1 and τ_e^2 as a function of a varying resistance with a mechanical speed of 90 rpm.

Shown in Figure 7.6 the estimate τ_e^2 is more affected by the Simulink model parameter variation than τ_e^2, an expected result. However, even if there occur a spike at a resistance of 1.7 Ω, τ_e^2 has a fairly constant amplitude, making the over all difference between $\tau_{l,app} + B\omega$ and τ_e^2 constant due to the simulated system being current controlled. With an increase in winding resistance, the PWM voltage compensate and gain a higher average value in order to provide the required current. This behaviour can also be concluded as the maximum deviation in Figure 7.6 is 0.7%, which is small in comparison to the resistance variation. Thereby, a variation in all resistive components will not contribute to a large variation in the estimates.

During the second test the resistance value affecting the power loss was varied to compare a calculation of τ_e^2 with a resistance deviating from the value used in the Simulink model. The Simulink model winding resistance was held constant at 1.4 Ω while changing the resistance in (7.2) from 1 Ω to 2 Ω. Except for $R = 1.4\Omega$, the second test had the same parameter settings as described in Table 7.3. The variation in τ_e^2 is shown in Figure 7.7 together with the total load $\tau_{l,app} + B\omega$.

In Figure 7.7 a linear decrease in the estimated motor torque is depicted. This is expected as the average current is assumed to be constant over the two evaluated periods and that the power loss term in (7.2) is linearly dependent on resistance, resulting in the curve slope. A similar reason can be applied to τ_e^1 which is directly dependent on the measured motor value Ψ_M. This value act as a pure gain in the system and a parameter variation of that component will have a linear affect of τ_e^1 as well.
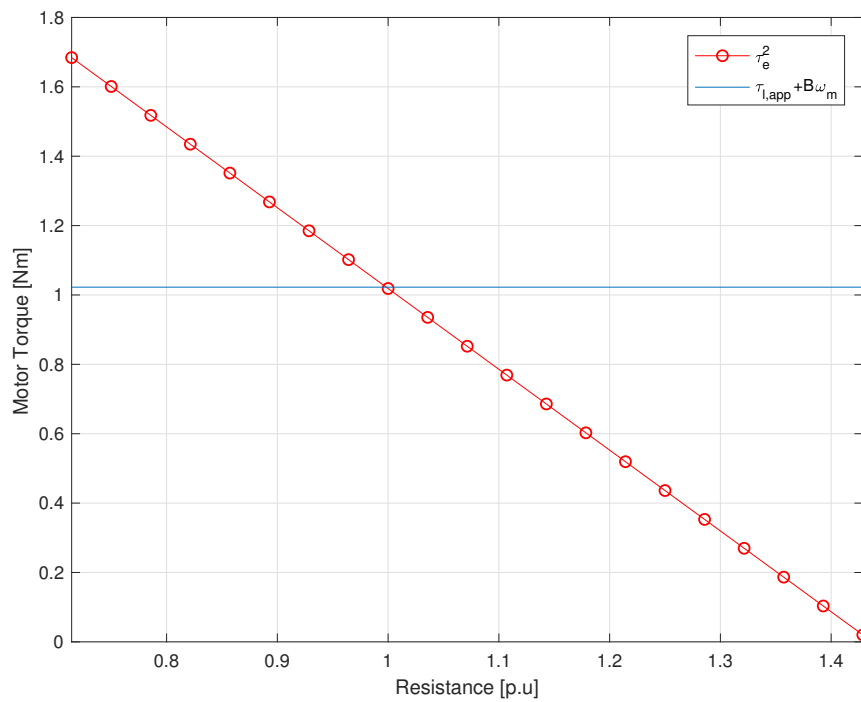
Figure 7.7: Resistance variation in the power loss calculation affecting the estimated motor torque calculated by τ_e^2 and compared to the total applied load torque. The resistance is defined in p.u. based on the measured winding resistance of 1.4 Ω

7.2.3   Rotor Speed And Position Sensor Resolution

Within a simulation environment the presence of external noise and sampling frequencies of sensors are neglected. In the real stepper motor system components such as speed and position sensors depend on sampling time and possible resolution consequently making their determination imprecise. By introducing a random noise in the simulation system the algorithm's noise tolerance can be observed, from which required sensor resolution can be determined. As the estimate τ_e^1 is position dependent and τ_e^2 speed dependent, noise on both individual components need to be added and their corresponding impact on the evaluated estimates. When conducting the simulation test the model parameters described in Table 7.4 were applied in the system. The varying parameters were the noise levels and the mechanical speed.

Table 7.4: Parameter setting for simulation measurement comparing motor torque algorithms with position and speed noise.

V_{in}	48 V
$I_{in,rms}$	2.8 A
R	1.4 Ω
ω_m	90 rpm
$\tau_{l,app}$	1 Nm
B	0.0024 Nms/rad

In order to obtain the desired information the noise level was implemented in the Simulink model. Simulink block Uniform Random Number was applied in the model to return a random number within a defined range. As the noise only should impact the output and not affect the mechanical behaviour of the motor, the Uniform Random Number block was added to the output signal before extraction. Because τ_e^1 is position dependent and estimate τ_e^2 speed dependent, disturbances were attached to respective components. Noise levels ranging $\pm 0.5 \cdot 10^{-4}$ to $\pm 0.5 \cdot 10^3$ were applied to the system and the resulting torque estimates were evaluated using the disturbed sensor signals. The different torque estimates with noise implemented were compared to corresponding ideal conditions with no implemented disturbance. Figure 7.8 show the results obtained from noise simulations with a mechanical speed of 90 rpm. The figure show the estimated torque deviation in percentage compared the individual torque values when no noise was applied to the system. According to Figure 7.8, a noise with a value higher than $\pm 0.5 \cdot 10^{-2}$ will affect the τ_e^1 estimation. A noise level of $\pm 0.5 \cdot 10^1$ can be applied to the system before τ_e^2 deviates. However, both algorithms have to be evaluated individually as the signals with applied disturbance has different nominal values.

A summary of the noise dependencies is shown in Table 7.5, where the mechanical speed, its corresponding electrical speed, the maximum allowed noise level before deviation and the required mechanical resolution are presented. Position dependent estimator τ_e^1 has a maximum noise level determined to $\pm 0.5 \cdot 10^{-2}$. As the electrical position varies between 0 and 2π rad, a noise of $\pm 0.5 \cdot 10^{-2}$ is calculated
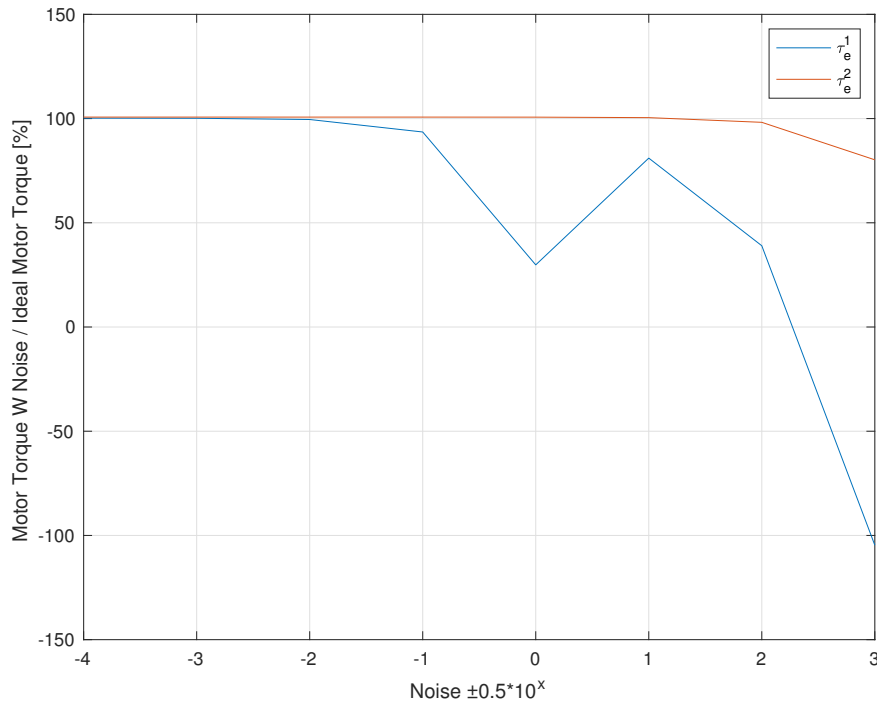
Figure 7.8: Relation in percentage between τ_{e^1} and τ_{e^2} when noise is and is not applied with a mechanical speed of 90 rpm. The applied noise levels reach $\pm 0.5 \cdot 10^{-4}$ to $\pm 0.5 \cdot 10^3$.

to its corresponding mechanical resolution in degrees as

$$\text{Mechanical Resolution} = \pm \frac{0.5 \cdot 10^{-2}}{2\pi} 360° \cdot \frac{1}{50}. \tag{7.3}$$

The term $\frac{1}{50}$ in (7.3) represent the transformation from electrical degrees, considering the number of rotor teeth. The required mechanical resolution for 90 rpm is 0.006° as seen in Table 7.5. Angular resolution denotes the allowed difference between the sampled current and rotor angle in order to obtain a correct motor torque estimate.

If instead exposing the system to a noise level of $\pm 0.5 \cdot 10^{-1}$, i.e. a position sensor with a resolution of 0.06°, the error increase to 6.64%. Further increasing the noise to $\pm 0.5 \cdot 10^0$ result in an error of 70% during 90 rpm operation, a larger error than the 20% error margin defined by LK Valves. Table 7.5 present the resolution of sensors with results from Figure 7.8. Figure 7.8 also show a maximum allowed disturbance level of $\pm 0.5 \cdot 10^2$ for τ_e^2, which translated from electrical rad/s to an error in mechanical speed of ± 477.5 rpm, an interesting result as the reference speed was 90 rpm.

A further investigation of the speed observed by the simulated sensor result in the values described in Table 7.6. According to Figure 7.8 and Table 7.6, a difference in reference and observed mean speed can be 90.39 rpm without disturbing the motor torque estimation. This means even if a mean sensor speed is twice as high as the reference during 90 rpm operation, according to Figure 7.8, the difference will

only be 1.8%. The unexpected result presented in Table 7.6 is due to the mean value of approximation of the extracted parameters being used when calculating τ_e^2, i.e. by averaging the noise the impact on the calculation will be smaller. If instead using the extracted values directly in (7.2) and thereafter calculating the mean of the two extracted periods, another result in required resolution would probably be obtained. However, the result provided in Table. 7.6 show that an implementation using averaged values of speed will depend less on the speed resolution up to 477.5 rpm or a noise level of $\pm 0.5 \cdot 10^2$. Even so, the most correct and probable resolution in implementation would be ± 4.77 rpm, which in noise levels refer to $\pm 0.5 \cdot 10^0$.

Table 7.5: Result from maximum position and speed sensor noise and corresponding resolution when $\omega_m = 90$ rpm.

	Mechanical Speed	Electrical Speed	Noise	Mechanical Resolution
τ_e^1	90 rpm	471.2 rad/s	$\pm 0.5 \cdot 10^{-2}$	0.006°
τ_e^2	90 rpm	471.2 rad/s	$\pm 0.5 \cdot 10^2$	$\pm$ 477.5 rpm

Table 7.6: The resulting reference speed and mean sensor speed from tests where noise is applied to the system.

Applied Noise	$\pm 0.5 \cdot 10^0$	$\pm 0.5 \cdot 10^1$	$\pm 0.5 \cdot 10^2$	$\pm 0.5 \cdot 10^3$
Reference Speed [rpm]	90	90	90	90
Mean Sensor Speed [rpm]	90.91	99.03	180.39	993.13
Speed Difference [rpm]	0.91	9.03	90.39	903.13

7.2.4 Reference Versus Simulated Rotational Speed

To further simplify an implementation, the controller's reference rotational speed could be used to calculate τ_e^2 rather than using a speed sensor. Simulating the model with the same parameter values as in Table 7.2 give the results shown in Figure 7.9 and Figure 7.10, the difference between the simulations being supply voltage. Shown in the two figures are the difference between calculating τ_e^2 using the reference speed and calculating τ_e^2 with the simulated speed. A lower supply voltage result in an outlying deviation of 1.5 Nmm due to resonance at approximately 120 rpm, not included in the plot to instead clearer view the smaller deviations. Except this outlying value, the methods of calculating τ_e^2 does not differ more than 0.08%. Increasing the supply voltage to 48 V results in an even smaller difference as shown in Figure 7.10, except for an increased, again not included, outlying differential spike due to resonance at 100 rpm measured to 19 Nmm. Neglecting the outlying value, the largest deviation occur at 110 rpm where the difference between the reference and measured speed was determined to 0.018%.
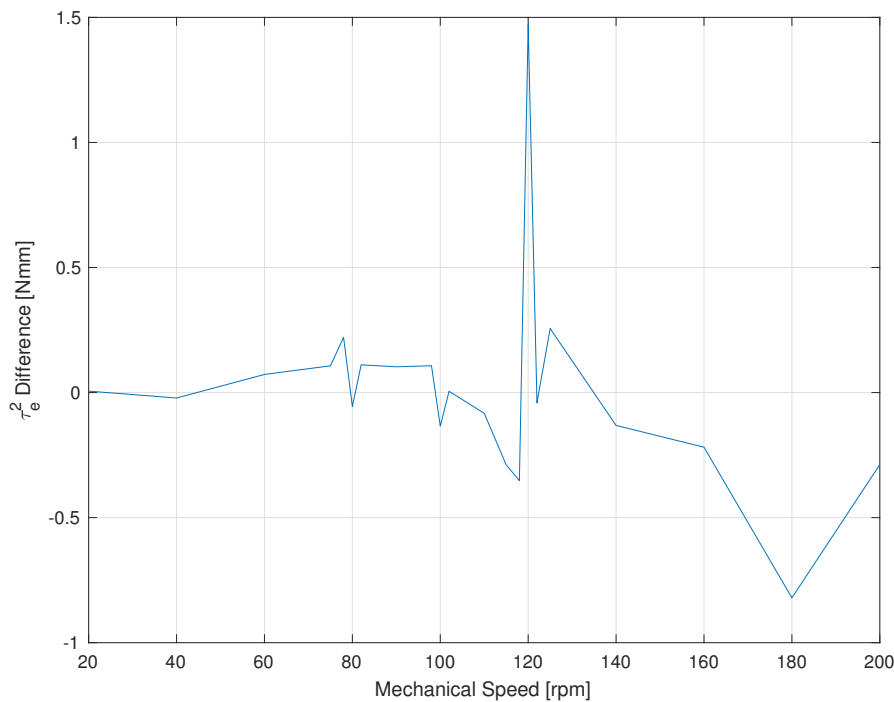
Figure 7.9: Difference in calculating τ_e^2 using the reference speed or calculating τ_e^2 using the simulated speed when the supply voltage is 24 V. The outlying spike at 100 rpm has a value of 1.5 Nmm.
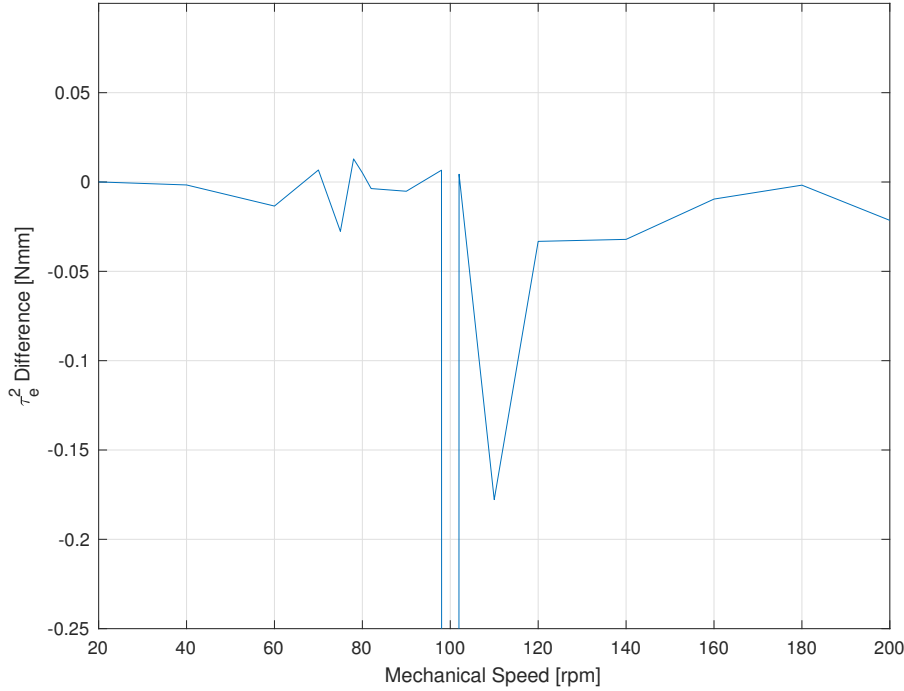
Figure 7.10: Difference in calculating τ_e^2 using the reference speed or calculating τ_e^2 using the simulated speed when the supply voltage is 48 V. The outlying spike at 120 rpm has a value of 19 Nmm.

7.3 Load Torque Assuming Constant Speed

To simplify the load torque estimation algorithm a comparison between the load torque when based on τ_e^1 and τ_e^2 were done while assuming a constant mechanical speed. Thereby, the mechanical dynamics described in (3.2), reproduced as

$$\tau_l = \tau_e - \tau_d(\theta_e) - J\frac{d\omega_m}{dt} - B\omega_m, \tag{7.4}$$

is reduced to (3.3), re-formulated as

$$\tau_l = \tau_e - \tau_d(\theta_e) - B\omega_m, \tag{7.5}$$

simplifying the expression as no derivative need to be taken into consideration. An investigation of this relation is of importance as a simplified expression would facilitate the execution in hardware.

During simulations, the Simulink configurations presented in Table 7.7 were applied showing only the varying factor during the tests being $\tau_{l,app}$. The simulations provided both τ_e^1 and τ_e^2 which were inserted in (7.5) where the corresponding $\tau_{l,app}$ for each motor torque algorithm were estimated and compared to the real applied load torque for evaluation of their accuracy.

Differences between the applied load torque $\tau_{l,app}$ and the estimated load torques $\tau_l(\tau_e^1)$ and $\tau_l(\tau_e^2)$ are displayed in Figure 7.11, showing the largest difference of 5.3% held by $\tau_l(\tau_e^2)$ when the applied load is 0.2 Nm, decreasing with an

Table 7.7: Parameter setting for simulation measurements assuming a constant speed.

V_{in}	48 V
$I_{in,rms}$	2.8 A
R	1.4 Ω
ω_m	90 rpm
$\tau_{l,app}$	0 – 3.3 Nm
B	0.0024 Nms/rad

increased load torque to after 0.6 Nm not exceed a deviation of 0.7%. The error of $\tau_l(\tau_e^1)$ is much smaller and overestimate the load torque with a deviation of 0.1% at 1 Nm.
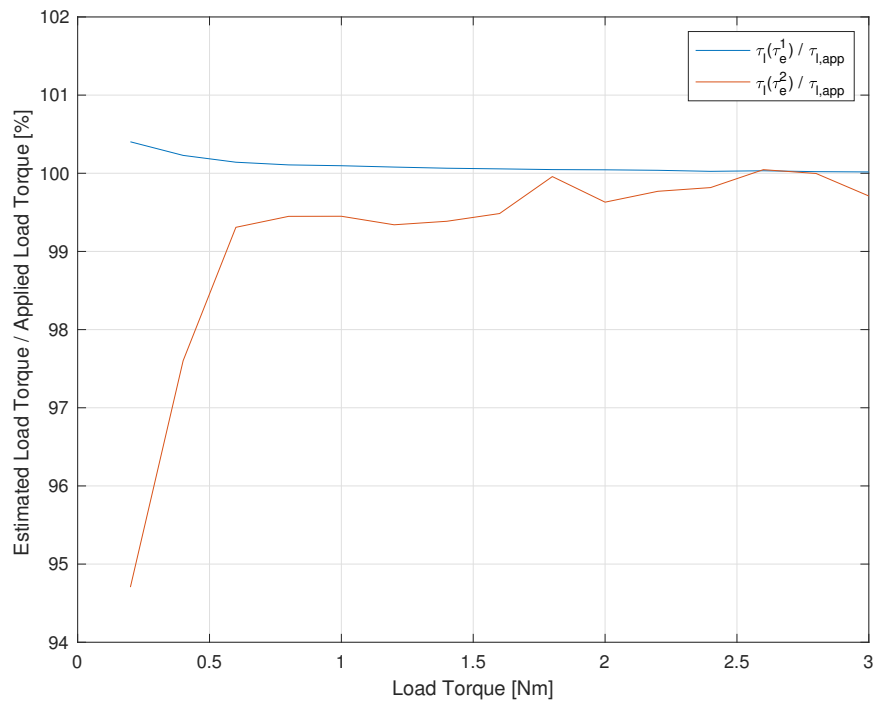
Figure 7.11: Relation in percentage between estimated and applied load torque assuming a constant speed of 90 rpm, for the both $\tau_l(\tau_e^1)$ and $\tau_l(\tau_e^2)$.

7.4 Load Torque Estimation During Worst Case Operation

Evaluations of the load torque estimates during non ideal conditions are essential in order to establish a range in which the estimates are reliable and well functioning. It is also important to investigate the system during a set of worst case scenarios as a contemporary parameter deviation may affect the motor model behaviour differently than when only considering individual deviations.

Two different simulations were done in order to provide information regarding the estimates behaviour. The first simulation conclude a variety in load torque having a constant speed while the second regard a constant load torque and speed parameter variation. In both tests extraction of the necessary estimate parameters were done during steady state operation and the assumption of constant mechanical speed, why the term $J\frac{d\omega_m}{dt}$ become zero. In addition, the detent torque component was also neglected as the mean value over the last two simulation periods is close to zero. A detailed description of the simulation parameter settings for respective test is shown in Table 7.8. In order to provide reasonable results for $\tau_l(\tau_e^2)$, the speed disturbance was set to $\pm 0.5 \cdot 10^0$, indicating a required sensor resolution of ± 4.77 rpm. During the simulations τ_e^1 and τ_e^2 were estimated with a 10% error in the Ψ_M and resistance value as noted in Table 7.8.

Table 7.8: Parameter setting for worst case simulations.

	Speed Variation	Load Torque Variation
V_{in}	24 V	24 V
$I_{in,rms}$	2.8 A	2.8 A
R_{model}	1.4 Ω	1.4 Ω
$R_{\tau_e^2}$	1.54 Ω	1.54 Ω
$\Psi_{M,model}$	0.8247 Wb	0.8247 Wb
Ψ_{M,τ_e^1}	0.907 Wb	0.907 Wb
ω_m	0-200 rpm	90 rpm
$\tau_{l,app}$	1 Nm	$0-3$ Nm
B	0.0024 Nms/rad	0.0024 Nms/rad
Noise θ_e	$\pm 0.5 \cdot 10^{-2}$	$\pm 0.5 \cdot 10^{-2}$
Noise ω_m	$\pm 0.5 \cdot 10^0$	$\pm 0.5 \cdot 10^0$

Results from the first test are shown in Figure 7.12 presenting the difference in percentage between the estimated load torques $\tau_l(\tau_e^1)$ and $\tau_l(\tau_e^2)$ and the applied load torque $\tau_{l,app}$, where the estimated load torques both are comprised by the estimated motor torque and the speed dependent torque component $B\omega$. The figure shows a constant $\tau_l(\tau_e^1)$, independent on the applied torque but with an overestimation of approximately 10% which is explained by the +10% error of Ψ_M. In comparison, the estimation of $\tau_l(\tau_e^2)$ is clearly dependent on the applied load. This is explained by, due to the constant current amplitude and resistance, the loss component in the
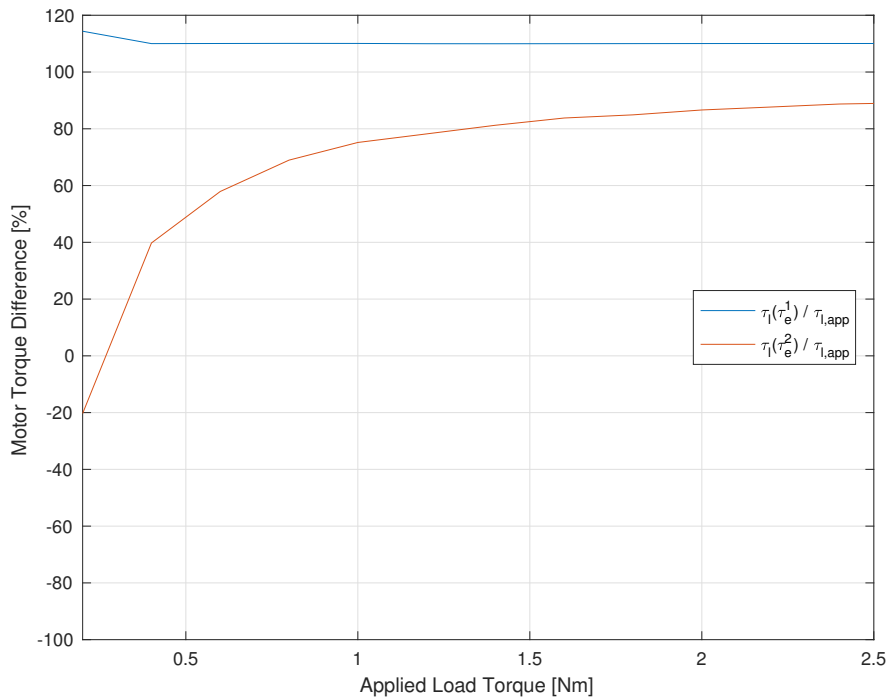
Figure 7.12: Relation in percentage between $\tau_l(\tau_e^1)$ and $\tau_l(\tau_e^2)$ varying the load torque during worst case parameter settings.

estimation being constant and overestimated, making its influence on $\tau_l(\tau_e^2)$ high, especially during low torque levels. Estimate $\tau_l(\tau_e^2)$ become better when increasing the applied load torque, reaching a difference of 11% compared to the total applied load torque.

The results from the second test is shown in Figure 7.13. The figure illustrates the difference in percentage between the estimated load torques and the applied load torque $\tau_{l,app}$ during different speed settings. Similar to the result in the first test, estimation method $\tau_l(\tau_e^1)$ is more accurate and stable than $\tau_l(\tau_e^2)$, who show a large deviation for lower speed settings due to the speed error being more prominent during lower speeds. Due to it overestimating during the higher speeds $\tau_l(\tau_e^1)$ would in an implementation for health monitoring provide a more secure system. Even though the estimation of $\tau_l(\tau_e^2)$ approach the applied load torque in both Figure 7.12 and Figure 7.13, the estimate provide a minimum deviation of 11% and 3.2% for the first respectively the second test. During the second test, and shown in Figure 7.13, $\tau_l(\tau_e^1)$ is behaving similarly as in the first test, with a constant overestimation of approximately 10%.
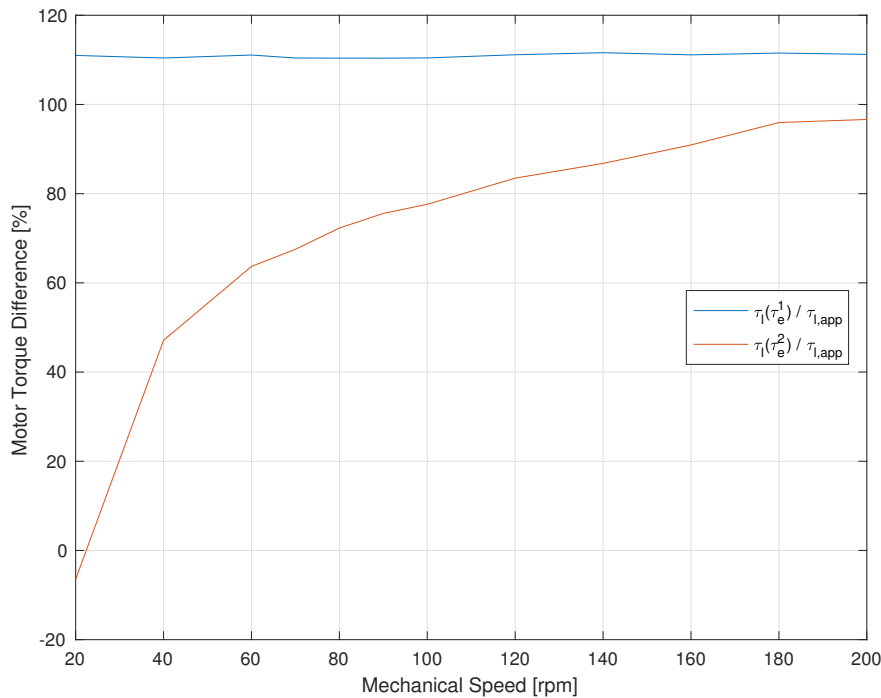
Figure 7.13: Relation in percentage between $\tau_l(\tau_e^1)$ and $\tau_l(\tau_e^2)$ varying the speed during worst case parameter settings.

7.5 Discussion

Finding a suitable load torque estimator depends both on accuracy and convenience in implementation. Limiting the implemented components will both reduce the price together with restraining the number of possible failing component. The possible options for estimating the load torque, e.g. using motor torque estimator τ_e^1 or τ_e^2, are therefor compared regarding specifications of the algorithms and necessary sensors.

To evaluate the Simulink model results τ_e^1 was compared with a curve in datasheet [20] regarding motor module PD60-4-1160 from Trinamic. The results suggest the τ_e^1 estimator to be similar to Trinamic's own curve. It is however impossible to conclude if the Simulink model is being correct in terms of maximum torque due to the limited information existing around Trinamic's data extraction. We do for example not know if the data from Trinamic is extracted from simulations or measurements on the real motor and if there exist individual changes between motors. It is moreover difficult to confirm the exact moment of error occurring in the simulation environment making the extracted torque value slightly higher than they would in a real case setup. Therefor the shape of the simulated curve and the curve provided by Trinamic were compared by pattern rather than exact output torques. Optimally, a comparison between the physical motor and its simulated version should be executed with furthermore extensive tests. This was however not possible to obtain due to the physical motor not being able to produce the desired

torque at given speeds.

The two motor torque equations τ_e^1 and τ_e^2 were compared to a total load torque $\tau_{l,app} + B\omega_m$ to investigate their accuracy. Simulation results indicates that the two methods both are accurate, however with a favour to τ_e^1 being the most correct estimator of the two. Not surprisingly, due to it being derived from the electrical motor definition. The two motor torque equations do however not differ more than 1.1% in test scenarios with optimal conditions having a supply voltage of 48 V. Implementing τ_e^1 requires a current sensor and position sensor not deviating in sampling more than 0.006° in order to provide an error smaller than 6.6%. Such an implementation additionally requires a measurement of Ψ_M for each individual motor. This parameter is important to accurately determine as it acts as a gain in (7.1), i.e. in an implementation with a 10% incorrect Ψ_M τ_e^1 will have an equally large error.

An implementation of τ_e^2 requires current and voltage sensors for each phase. Due to the winding current being controlled by PWM it is easy to extract the voltage level directly from the controller using the reference voltage. Thereby the need for voltage sensors is eliminated. A correct measurement of the resistance is important as this, similar to Ψ_M, act as a linear component in the estimate. An implementation of τ_e^2 additionally requires a mechanical speed sensor with an accuracy of ± 4.77 rpm. Results proved a worse resolution could be managed if the algorithm is implemented using the mean of the speed during a larger time interval. According to Figure 7.9 and Figure 7.10, the difference of calculating τ_e^2 using the reference speed versus measured speed is only 0.08% and 0.018%, with the smaller value corresponding to the larger supply voltage. An increased supply voltage in other words decrease the difference in calculating τ_e^2 with the reference speed compared to the measured speed. Both cases result in a difference from which an assumption of using the reference speed rather than using a speed sensor is reasonable in order to simplify an implementation of τ_e^2. Due to the dependency of ω_m when calculating τ_e^2, it is not possible to estimate the load torque when the speed is 0, i.e. in the opening and closing moment of the valve. As the estimation of load torque in this thesis concern a valve where the interesting torque to estimate is the maximum value during an opening and closing period of $13 - 60$ seconds, an alternative of not to measure τ_e during a specified first and last time interval is acceptable. A conclusion of the individually required sensors for τ_e^1 and τ_e^2 are defined in Table 7.9. Maximal flux linkage Ψ_M, the number of rotor teeth N_r and winding resistance R are motor specific and defined as constants in the implementation.

Ultimately the load torque estimation τ_l which use either of the two alternatives of calculating τ_e is evaluated. Simplifying the expression by assuming a constant speed and thereby neglecting the equation derivative results in an inaccurate τ_l estimation up to 0.1% for $\tau_l(\tau_e^1)$ and 0.7% for $\tau_l(\tau_e^2)$, having a load torque larger than 0.6 Nm in the latter case. With a load torque below 0.6 Nm $\tau_l(\tau_e^2)$ has an deviation up to 5.3%. However, with a gearbox with ratio 84:1, a produced motor torque of 0.6 Nm result in a torque of 50 Nm at the load which is only one fifth of the max holding torque required by the motor according to LK Valves. As the interesting torque to estimate is much higher than this breaking point of 50 Nm, this result is determined to be insignificant for estimations. The detent torque can

Table 7.9: Comparisons of necessary parameters measurements and sensors needed for the two methods to calculate τ_e

	τ_e^1	τ_e^2
Current Sensor	x	x
Voltage sensor		
Rotor position sensor	x	
Rotor speed sensor		
Ψ_M	x	
N_r	x	
R		x

additionally be neglected in (7.4) due to it being periodical within a teeth alignment making it an average zero. Such an assumption further simplifies the load torque estimation algorithm as it neglects another position dependent variable.

During the worst case simulations the estimator $\tau_l(\tau_e^1)$ provides a more stable result than $\tau_l(\tau_e^2)$ due to it providing a constant 10% overestimation of the load torque. Estimator $\tau_l(\tau_e^2)$ provide large errors during low mechanical speeds due to the speed dependency in (7.2). With a low mechanical speed an error in speed accuracy will have a more significant impact on the estimation. However, by increasing the speed the deviation of $\tau_l(\tau_e^2)$ will decrease with the two estimates both providing an error of 10% at 150 rpm. It is clear, that for an implementation the use of accurate parameters are more important considering $\tau_l(\tau_e^2)$ compared to $\tau_l(\tau_e^1)$.

We suggest that in order to improve the accuracy of the models 48 V should be applied as a supply voltage, the necessary sensors should have a satisfying resolution. Further, parameters Ψ_M and R used in the estimates of motor torque should be accurately measured for each motor. We also want to emphasise that every system has unique parameters and behaviour that needs to be determined before an implementation.

8

Conclusion

By estimating the load torque of a valve controlled by a hybrid stepper motor, the mechanical health of the system could be determined. A study has been made to provide and evaluate algorithms for load torque estimation, using only motor parameters. Two motor torque estimations have been evaluated, together with simplifications of the load torque expression, in order to determine a suitable algorithm to implement in the valve control system.

Due to the presented results of error deviations and the fewer required sensors in an implementation compared to the other option as presented in Table 7.9, the suggested method to estimate the load torque of the valve control system is expressed as

$$\tau_l = \frac{V_A i_A + V_B i_B - (R_A i_A^2 + R_B i_B^2)}{\omega_m} - B\omega_m, \qquad (8.1)$$

which is a combination of the motor torque estimate τ_e^2 and the assumption of constant mechanical speed while neglecting the detent torque. The detent torque is negligible due to it being periodical, having an average of zero. Based on the simulation results the assumption of constant speed resulted in an underestimation for τ_e^2 of 5.3% during an applied load of 0.2 Nm. However, for applied load torques above 0.6 Nm the estimate did not differ more than 0.7%. During all load torque levels applied to the system during the simulation the estimate τ_e^1 had a maximum deviation of 0.1%, making the assumption of constant speed reasonable for both cases for applied load torques above 0.6 Nm. Noted in (8.1) the estimate depend on the $B\omega_m$ term, in turn depending on the mechanical system and mechanical speed. For systems with a low B value, the term can be neglected, further reducing (8.1). However, measurements and determination of B are necessary in order to conclude the term to be neglected. It is additionally important to implement the estimator using a high voltage, a well defined resistance and not estimating the load torque during the closing and opening moment of the valve to provide a well functioning algorithm.

During the last test the system was put in a worst case scenario, where the estimates were evaluated during operation with low supply voltage, a 10% overestimation of Ψ_M and R in calculations, as well as the assumption of having a mechanical speed sensor with the resolution of 4.77 rpm and a mechanical position sensor with an accuracy of 0.006°. According to the results, the load torque estimation $\tau_l(\tau_e^1)$ had a constant overestimation of 10% for variations in both speed and applied load. This overestimation is due to the implemented error in Ψ_M, making it important to accurately measure the component if that estimation is to be used. For $\tau_l(\tau_e^2)$ the load estimation was not acceptable for both low speed levels and applied load,

whereas the difference between the real and estimated load torque in percentage for 90 rpm and 1 Nm operation was 24%. However, as the reason for the large underestimation of $\tau_l(\tau_e^2)$ is due to the direct impact on speed and resistance, the mechanical speed and accurate measurements of winding resistance important parameters to extract correctly when implementing the estimate. Due to the knowledge LK Valve possess regarding the specific system and that the algorithm with this knowledge can be altered for specific implementations, we assume this worst case scenario to have a low probability of occurring.

Thereby, this study proves it theoretically possible to estimate the load torque within reasonable error margins in a valve control system based only on parameters from a 2-phase bipolar stepper motor. Before an algorithm implementation measurements on the intended motor need to be conducted. Motor parameters such as winding resistance, winding inductance and maximum flux linkage are motor dependent and the conclusions drawn in this thesis only being valid for module PD60-4-1160 from Trinamic. With a torque sensor on the load, the measured and estimated τ_l can be compared to determine if the estimation is acceptable outside the simulated environment. If the results are accurate, the estimation of τ_l is implemented in hardware to be calculated in a real time system. Questions regarding a hardware implementation require further investigation in order to obtain an optimal mechanical health monitoring system.

Bibliography

[1] K. V. Arzhanov and Y. A. Shurygin, "Energy saving control algorithms of stepper motor drives for metal-working machines equipped with cnc unit," in *2015 International Conference on Mechanical Engineering, Automation and Control Systems (MEACS)*, pp. 1–4, 2015.

[2] A. H. et. al., *Electric motors and drives: fundamentals, types, and applications.* Amsterdam: Elsevier/Newnes, fourth ed., 2013.

[3] P. Acarnley, *Stepping motors: a guide to theory and practice*, vol. 63. London: Institution of Electrical Engineers, 4.;4; ed., 2011.

[4] S. E. Mirbagheri, M. Al-Bassyiouni, and A. Dasgupta, "Bearing wear model for optical disk drive stepper motor," pp. 1274–1280, IEEE, 2012.

[5] F. Khorrami, P. Krishnamurthy, and H. Melkote, "Modeling and adaptive nonlinear control of electric motors," 2003.

[6] B. C. Kuo, *Stepper motor.* 2014.

[7] K. V. Manning, "Reluctance," 2014.

[8] P. Zaskalicky and M. Zaskalicka, "Analytical method of calculation of the current and torque of a reluctance stepper motor using fourier complex series," pp. 899–902, IEEE, 2008.

[9] T. Kenjo, *Stepping motors and their microprocessor controls.* Oxford University Press, New York, 1984.

[10] H. K. et. al., *Small Electric Motors.* Institution of Engineering and Technology, 1998.

[11] M. Zribi and J. Chiasson, "Position control of a pm stepper motor by exact linearization," *IEEE Transactions on Automatic Control*, vol. 36, no. 5, pp. 620–625, 1991.

[12] B. Henke, O. Sawodny, S. Schmidt, and R. Neumann, "Modeling of hybrid stepper motors for closed loop operation," *IFAC Proceedings Volumes*, vol. 46, no. 5, pp. 177 – 183, 2013.

[13] K. e. a. Ogawa, "Hydrodynamic characteristics of a butterfly valve — prediction of torque characteristics," *ISA Transactions*, vol. 34, no. 4, pp. 327–333, 1995.

[14] H. Grotstollen, "Optimal design of motor and gear for drives with high acceleration by consideration of torque-speed and torque-acceleration product," *IEEE Transactions on Industry Applications*, vol. 47, no. 1, pp. 144–152, 2011.

[15] C. Solliec and F. Danbon, "Aerodynamic torque acting on a butterfly valve. comparison and choice of a torque coefficient," *Journal of Fluids Engineering*, vol. 121, no. 4, p. 914, 1999.

[16] M. J. Morris and J. C. Dutton, "Aerodynamic torque characteristics of butterfly valves in compressible flow," *Journal of Fluids Engineering*, vol. 111, no. 4, p. 392, 1989.

[17] B. Nesbitt, S. (e-book collection), E. C. (e-book collection), and K. (e-book collection), *Valves manual international: handbook of valves and actuators*. Burlington, MA;Oxford;: Butterworth-Heinemann, 1st ed., 2007;2011;.

[18] P. C. Krause, O. Wasynczuk, S. D. Sudhoff, and S. Pekarek, *Theory of Electromechanical Energy Conversion*, vol. 75, pp. 1–52. Hoboken, NJ, USA: Wiley, 3 ed., 2013.

[19] Trinamic, "QMOT QSH6018 manual." `https://www.trinamic.com/fileadmin/assets/Products/Motors_Documents/QSH6018_manual.pdf`, 2014. [Online; accessed 25-May-2018].

[20] Trinamic, "Hardware manual PD-1160." `https://www.trinamic.com/fileadmin/assets/Products/Drives_Documents/PD-1160_hardware_manual.pdf`, 2013. [Online; accessed 25-May-2018].

[21] Trinamic, "Firmware manual PD-1160." `https://www.trinamic.com/fileadmin/assets/Products/Drives_Documents/PD-1160_TMCL-firmware_manual_V104.pdf`, 2017. [Online; accessed 25-May-2018].

[22] Trinamic, "TMC262 datasheet." `https://www.trinamic.com/fileadmin/assets/Products/ICs_Documents/TMC262_Datasheet.pdf`, 2016. [Online; accessed 25-May-2018].

[23] Trinamic, "TMC424 datasheet." `https://www.trinamic.com/fileadmin/assets/Products/ICs_Documents/TMC429_datasheet.pdf`, 2015. [Online; accessed 25-May-2018].

[24] PEAK Electronic Design ltd, "Atlas LCR Model: LCR40, Product Breef," 2012.